1. COVER PAGE DATA ELEMENTS

a. Federal Agency and Organization Element to Which Report is Submitted:
US DEPARTMENT OF ENERGY
OFFICE OF FOSSIL ENERGY
NATIONAL ENERGY TECHNOLOGY LABORATORY

b. Federal Grant or Other Identifying Number Assigned by Agency:
DE-FE0031910

c. Project Title:
A TANDEM ELECTROLYSIS PROCESS FOR MULTI-CARBON CHEMICAL PRODUCTION FROM CARBON DIOXIDE

d. PD/PI Name, Title and Contact Information (e-mail address and phone number):
FENG JIAO, Professor of Chemical and Biomolecular Engineering, University of Delaware
150 Academy Street, Newark, DE 19716
TEL: (302) 831 3679
EMAIL: JIAO@UDEL.EDU

e. Name of Submitting Official, Title, and Contact Information (e-mail address and phone number), if other than PD/PI:
Elizabeth Townsend, Contract and Grant Specialist, University of Delaware
TEL: (302) 831 7274
EMAIL: townsend@udel.edu

f. Submission Date:
01/08/2024

g. DUNS Number:
05-900-7500

h. Recipient Organization (Name and Address):
UNIVERSITY OF DELAWARE
210 HULLIHEN HALL
NEWARK DE, 19716

i. Project/Grant Period (Start Date, End Date):
10/01/2020 – 07/31/2023

j. Reporting Period End Date:
07/31/2023

k. Report Term or Frequency (annual, semi-annual, quarterly, other):
Final

l. Signature of Submitting Official (electronic signatures (i.e., Adobe Acrobat) are acceptable)

EM Townsend

2. APPROACH

Electrode preparation. Reinforced GDL was fabricated by air-spraying Teflon dispersion FEPD 121 (Fuel Cell Store) and carbon black (Vulcan XC-72R; Fuel Cell Store) onto a Sigracet 39 BC GDL (Fuel Cell Store). FEP ink was first prepared by adding 400 mg carbon black and desired amount of FEPD (e.g., 10, 20, and 30 wt. % relative to carbon black) in 20mL IPA and 20 mL deionized (DI) water. After sonicating and vortexing for 30 min, FEP ink was air-sprayed onto the GDL at 100 °C until 20 wt.% relative to GDL was loaded. After drying, reinforced GDL was heat-treated at 300 °C in the pre-heated furnace for 10 min.

Cathodes were fabricated by air-spraying cathode ink onto the reinforced GDL. Ag ink was prepared by adding 100 mg Ag (<100 nm, 99.5%, Sigma-Aldrich), desired amount of carbon black, and Sustainion XA-9 ionomer (Dioxide Materials) to obtain 5 wt. % ionomer relative to Ag in 10 mL IPA and 10 mL DI water. Cu ink was prepared by adding 100 mg Cu (~625 mesh, 0.5-1.5 micron, 99%, Alfa Aesar), desired amount of carbon black, and Nafion ionomer (Fuel Cell Store) to obtain 10 wt. % ionomer relative to Cu in 10 mL IPA and 10 mL DI water. After sonicating and vortexing for 30 min, catalyst ink was air-sprayed onto the reinforced GDL at 100 °C to obtain 1.0 mg cm^{-2} loading.

IrO_2 (99.99%, Alfa Aesar) anode was fabricated by air-spraying IrO_2 ink onto Ti felt (Fuel Cell Store). IrO_2 ink was prepared by adding 50 mg IrO_2 and Teflon dispersion (FEPD 121) to obtain 15 wt. % FEP relative to IrO_2 into 5 mL DI water first, followed by 5 mL IPA. After sonicating and vortexing for 30 min, catalyst ink was air-sprayed onto the Ti felt at 200 °C to obtain 2.0 mg cm^{-2} loading. After drying, IrO_2 anode was heat-treated at 300 °C in the pre-heated furnace for 1 h. NiFe anode was prepared by following the previously reported procedure.[30] Essentially, Ni and Fe were electrodeposited onto Ni foam (99.99%, 1.6 mm thickness, MTI Corporation) in an electrolyte bath of 3 mM nickel (II) nitrate hexahydrate ($Ni(NO_3)_2 \cdot 6H_2O$, Sigma-Aldrich) and 3mM iron (III) nitrate nonahydrate ($Fe(NO_3)_3 \cdot 9H_2O$, Sigma-Aldrich).

Electrochemical experiment. CO_2 and CO electroreduction experiments were conducted in a MEA electrolyzer with serpentine flow channels. Teflon gaskets (0.01"; McMaster-Carr) were used to seal different components in the electrolyzer. For CO_2 electrolysis, Ag cathode, IrO_2 anode, Sustainion membrane (X37-50 Grade RT; Dioxide Materials), and 100 mM $CsHCO_3$ (Alfa Aesar) were used. For CO electrolysis, Cu cathode, NiFe anode, and 2 M KOH (Alfa Aesar) were used. For small-scale CO electrolysis AMX membrane (Orion Polymer) was used and for stack testing PiperION (A60-HCO3, Versogen) was used due to commercial availability. For the small-scale two-step tandem CO_2 electrolysis stability test, CO_2 was supplied at 8 mL min^{-1}, and NaOH pellet was used as a CO_2 trap. CO_2 trap was switched every 48 h. 50 mL of 100 mM $CsHCO_3$ was recirculated, and it was switched at 144 h and 264 h. 50 mL of 2 M KOH was switched every 24 h, and liquid samples were obtained either every 12 h or 24 h. Cathode side of CO electrolyzer was washed with 3 mL of DI water at 137 h and every 48 h starting at 168 h. Data was lost at ~100 h due to computer failure, but electrolysis was continuously operated. For the stack experiments, a powersource (Cosel, PCA1500F) was used to supply current to the electrolyzer and the current was distributed using a busbar (Blue Sea Systems, PowerBar 1000). For the 500 cm^2 CO_2 electroylsis stack, CO_2 was supplied at 1.8 L min^{-1} and for the 1,000 cm^2 CO electrolysis stack, CO was supplied at ~2.9 L min^{-1}. For contaminant testing at 200 cm^2, a total gas flowrate of 250 ml min^{-1} was supplied.

Product quantification. Gas products were quantified using a multiple gas analyzer no. 5 gas chromatography system (SRI Instruments), which was equipped with a MolSieve 5A column, a HaySep D column, and a thermal conductivity detector (TCD). Outlet gas flow rates were measured with an ADM flow meter (Agilent). Liquid products were quantified by ^{1}H-NMR. After diluting the liquid products in 2 M KOH by 1/20, 500 μL of the sample was mixed with 100 μL of 25 ppm (v/v) dimethyl sulfoxide (DMSO; 99.9%, Alfa Aesar) in D_2O, which was used as the internal standard.

Material characterization. SEM and EDS images were obtained with Auriga 60 CrossBeam (1.5 kV). High-resolution XPS measurements were performed with K-alpha Alpha X-ray photoelectron spectrometer system (Thermo Fisher Scientific, 20 eV pass energy, 0.1 eV step size). All spectra were calibrated to the adventitious carbon at 284.8 eV, and peak fitting was conducted with Thermo Avantage software.

Life Cycle Analysis and Techno-Economic Assessment. The life cycle assessment is done following the requirements in ISO 14044:2006 [1] and the guidelines [2], [3]: 1. Goal and scope definition, 2. Life cycle inventory analysis (LCI), 3. Life cycle impact assessment (LCIA), 4. Interpretation of the results. Following the Global CO_2 Initiative guidelines [10], the impact assessment methodology used in the life cycle analysis is TRACI (2.1, July 2012) to ensure comparability and geographical representativeness. The database used to retrieve the environmental impacts is the U.S. Life Cycle Inventory (USLCI) Database created by NREL and other partners. The entries missing in USLCI were gathered from EcoInvent v3.8.

The techno-economic assessment relied upon previously published electroylzer models. Cost relationships from these models were then coupled with a custom separation model generated in ASPEN Plus.

3. RESULTS AND DISCUSSION

Development of Nanostructured Cu Catalysts

Recent studies on electrochemical CO reduction reaction (CORR) using two-dimensional Cu nanosheets has demonstrated excellent selectivity towards acetate, which was attributed to selective exposure of Cu (111) facets [4]. Cu nanosheets are promising for CORR to acetate, so we investigated various synthesis parameters to establish a correlation between synthetic condition and material morphology.

In a typical synthesis, 0.1 g CTAB (Cetyltrimethylammonium bromide) was dissolved in 15 ml deionized water. After forming a homogeneous, clear solution, 50 mg copper nitrate trihydrate, 0.1 g HMTA (Hexamethylenetetramine) and 0.1 g L-ascorbic acid were added. Then the solution was kept in an oven at a desired temperature, ranging from 60 to 80 ˚C for 3 hrs. Because <10 mg of Cu nanosheets can be obtained from one synthesis, we scaled up the synthesis by 10 times: 1 g CTAB, 0.5 g copper nitrate trihydrate, 1 g HMTA and 1 g L-ascorbic acid in 150 ml deionized water. The synthesis step remained the same as the typical synthesis. The product was collected by centrifugation at 6000 rpm for 20 mins and washed with deionized water and ethanol three times to remove residue of the chemicals. The final product was then dried in a vacuum oven overnight to avoid further oxidation of the metallic copper.

As shown in SEM images, the crystal morphology is significantly influenced by the temperature (Fig. 1). Cu nanosheets maintained at 60 ˚C displays an asymmetric hexagonal configuration with nucleated seeds remaining from incomplete crystallization on top of the nanosheet, implying the insufficient thermal energy for crystal growth. Cu nanosheets maintained at 90 ˚C also shows overly large Cu nanosheets with numerous small Cu crystals on the surface, indicating that the crystallization at high temperature is not favorable. On the contrary, Cu nanosheets synthesized at 80 ˚C represents more homogeneous distribution of crystal shape with clear edges. Therefore, all nanosheets synthesized in this work was kept at 80 ˚C.

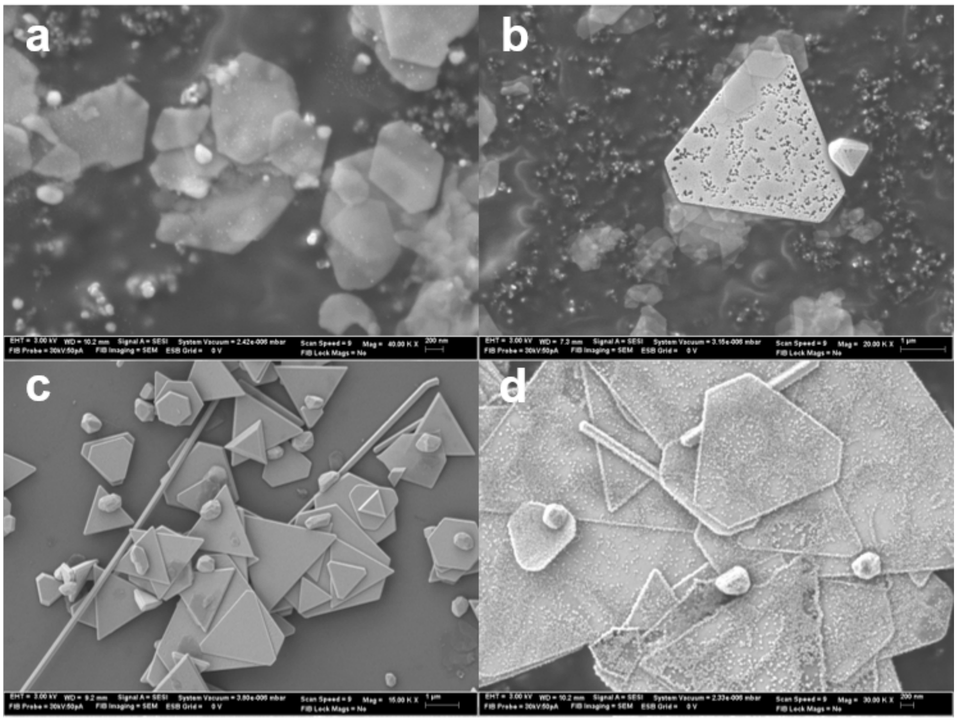

Figure 1. SEM images of Cu nanosheets synthesized at (a) 60℃, (b) 70℃, (c) 80℃, and (d) 90℃ with a scaled-up method.

Next, we examined the effect of iodide ions in Cu nanosheet morphology by adding 0, 20, and 40 μM of KI to the synthesis solution. Previous study on the influence of halide ion on gold particle formation has shown that iodide ions are inclined to be adsorbed on (111) facets leading to continuous lateral growth forming triangular shape in (111) direction [5]. Figure 2 clearly confirms that increasing iodide ions favors the oriented-growth toward Cu (111) direction shaping clear triangular nanosheet formation. In Figure 2a, Cu nanosheets without KI represents mixed forms of two-dimensional hexagons and triangles, whereas Cu nanosheets with 20 and 40 μM KI show majority of triangle morphology with clearer edges as shown in Figure 2b and c.

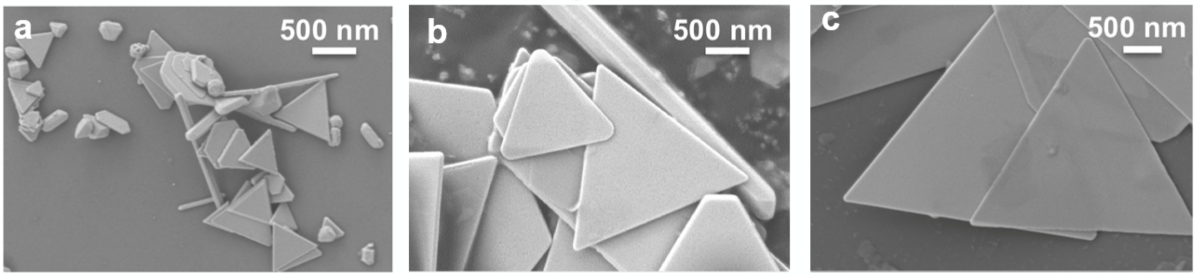

Figure 2. SEM images of Cu nanosheets synthesized with (a) 0 μM, (b) 20 μM, and (c) 0 μM KI.

Interestingly, the introduction of iodide ions has an impact on the size control. The edge length of the nanosheet tends to increase as the concentration of potassium iodide increases. It may be because more available iodide ions are absorbed onto the basal plane combined with cuprous ions corresponding to the further growth in the lateral direction. The edge length will be an interesting indicator to track the selectivity change in CO reduction with respect to the facet ratio as the increase in the edge length implies the high proportion of Cu (111) facet to other facets. CORR performance on various Cu nanosheets will be investigated next.

After optimizing the synthesis parameters, CuNS was successfully synthesized (Fig. 3a) and the length of the side was distributed in the range of 2-5 μm.

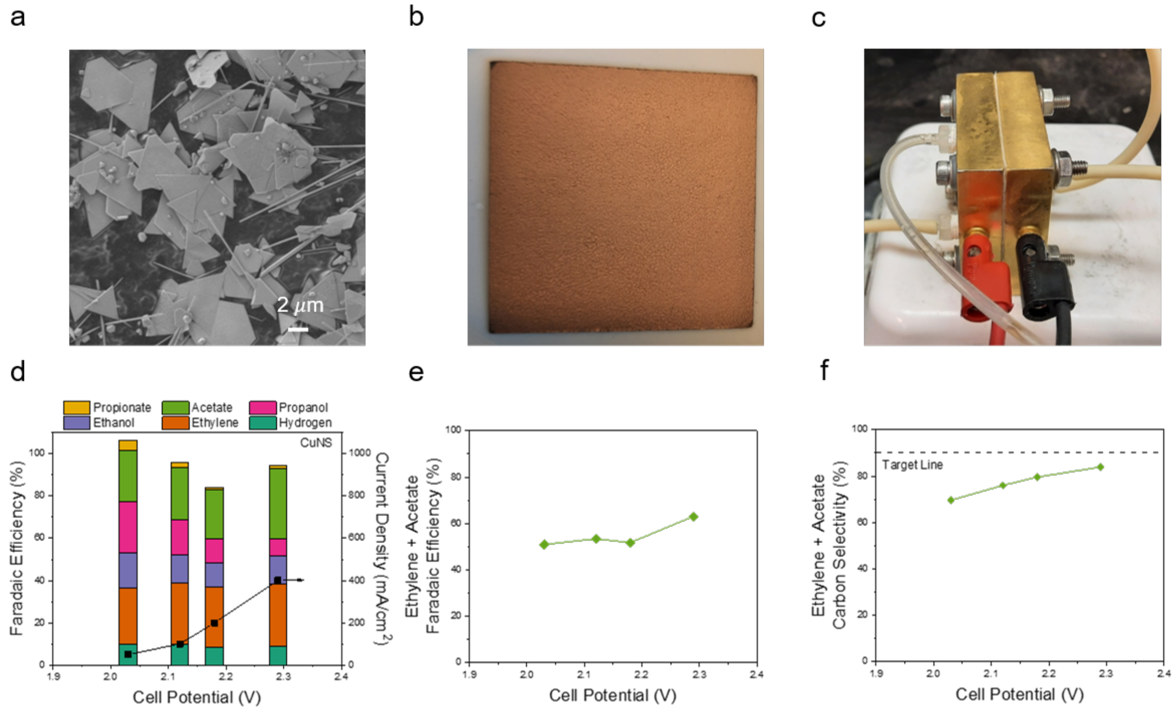

Figure 3. Cu nanosheet (CuNS) in CO electroreduction. (a) Scanning electron microscope image of CuNS synthesized, (b) CuNS electrode, and (c) Membrane electrode assemply (MEA) electrolyzer. (d) Faradaic efficiency and current density, (e) ethylene + acetate Faradaic efficiency, and (f) ethylene + acetate carbon selectivity vs. cell potential for CO electrolysis using CuNS.

CuNS ink was prepared by dispersing 45 mg of CuNS and 20 wt% nafion as a binder in 10 mL of 50:50 IPA:water. After sonicating for 30 min, the solution was air sprayed on a 39 BB sigaracet gas diffusion layer (GDL) to achieve 0.5 mg cm^{-2} loading of CuNS (Fig. 3b). CuNS was evenly coated on the GDL. CuNS electrode was then incorporated into a membrane electrode assembly (MEA) electrolyzer with an active area of 5 cm^2 (Fig. 3c) for CORR. FAA and NiFe foam were used as a membrane and an anode, repectively. CORR was performed under 2M KOH, 40 mL min^{-1} CO, 15.5 psia, and 35 ℃. Gas products were quantified via on-line gas chromatograph (GC). Liquid products were collected with the electrolyte and cold trap, which was installed at the exit gas stream, and quantified via ^{1}H nuclear magnetic resonance (NMR). CuNS achieved relatively good CORR performance (Fig. 3d), achieving high current density (>200 mA cm^{-2}) at low cell potential (<2.2 V). H_2 Faradaic efficiency (FE) was less than 10% and ethylene and acetate were the dominant CORR products over a wide range of potentials However, ethylene+acetate FE remained below 65% and their carbon selectivity did not reach the target, which was 90% (Fig. 3e and f).

To meet the target ethylene + acetate carbon selectivity of 90%, Cu nanoparticles (CuNP) of various sizes were evaluated for CORR. In the case of CuNP, 5wt% of Nafion binder was used since 5wt% was sufficient to bind CuNP onto the GDL. Keeping all other parameters consistent, CORR was performed using 1) 25 nm, 2) 40-60 nm, 3) 70 nm, and 4) 100 nm CuNP. As shown in Fig. 4a, higher current densities were achieved at lower cell potentials on all CuNP compared to CuNS. Because CuNP showed promising results, they were operated to higher current densities (up to 1 A cm^{-2}). Low H_2 FE and high CORR products FE were maintained over a wide range of potentials on all catalysts (Fig. 2b). Increase in H_2 FE and decrease in CORR products FE at high cell potentials may be due to CO starvation at the electrode surface induced by high reaction rates or greater overpotential which favors hydrogen evolution reaction. Regarding ethylene and acetate FEs (Fig. 4c and d), it appears that ethylene and acetate pathways compete with each other, and the enhancement of one comes at the expense of the other. For instance, 25 nm CuNP exhibited the highest ethylene FE and the lowest acetate FE. On the other hand, CuNS showed the lowest ethylene FE and one of the highest acetate FE. After evaluating various nanostructured Cu catalysts, 40-60 nm CuNP was determined to be the best catalyst for producing ethylene and acetate. It showed the highest ethylene + acetate FE and carbon selectivity (Fig. 4e and f), achieving 90% carbon selectivity at a relatively low cell potential of <2.2 V.

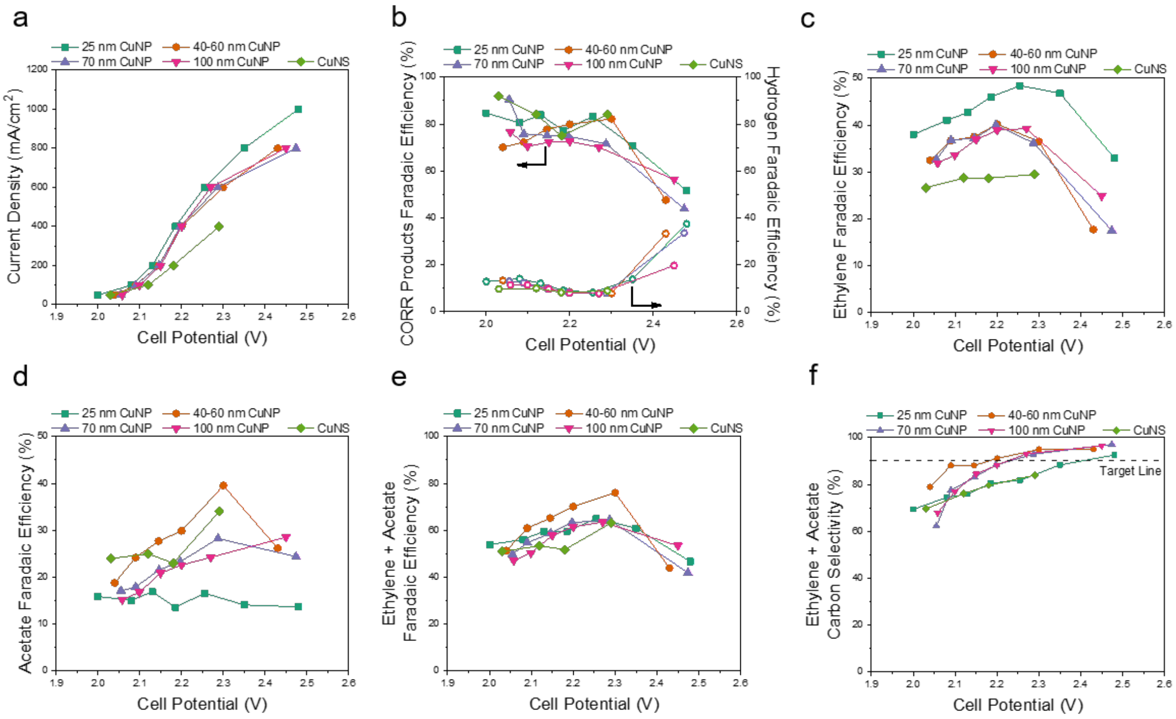

Figure 4. Comparison of various nanostructured Cu catalysts in CO electroreduction. (a) Current density, (b) CO reduction reaction (CORR) products Faradaic efficiency, (c) ethylene Faradaic efficiency, (d) acetate Faradaic efficiency, (e) ethylene + acetate Faradaic efficiency, and (f) ethylene + acetate selectivity vs. cell potential on 25 nm Cu nanoparticle (CuNP), 40-60 nm CuNP, 70 nm CuNP, 100 nm CuNP, and Cu nanosheet (CuNS).

CO electroreduction performance was stable over the span of the experiments presented here, which were typically between 3 and 5 hours. The spent catalysts were not analyzed since there was no sign of performance degradation.

Development of Anion-Exchange-Membrane-Based CO Electrolysis Reactor

Figure 5a and b show the cell performance of MEAs with various membranes. It can be seen that the impact of the membrane on the selectivity of the gas products (H_2 and C_2H_4) is negligible. On the other hand, the membrane properties affect the liquid product crossover. For example, high ethanol crossover was observed for the membranes with high ion exchange capacity (Fig. 5c). The ethanol in the anolyte stream is further oxidized from the anode electrode leading to high acetate production (Fig. 5c, d). The membranes with low ion exchange capacity demonstrated low alcohol crossover resulting in high alcohol and low acetate Faradaic efficiencies. The cell performance remains identical for all the examined MEAs when Ni foam was used as an anode. The similar faradaic efficiencies calculated in the Ni foam MEAs indicate that the anion exchange membrane has an indirect role in the observed selectivity of liquid products. The latest suggests that the membrane can tune the liquid product selectivity only when an active electrode for alcohol electrooxidation is used as an anode.

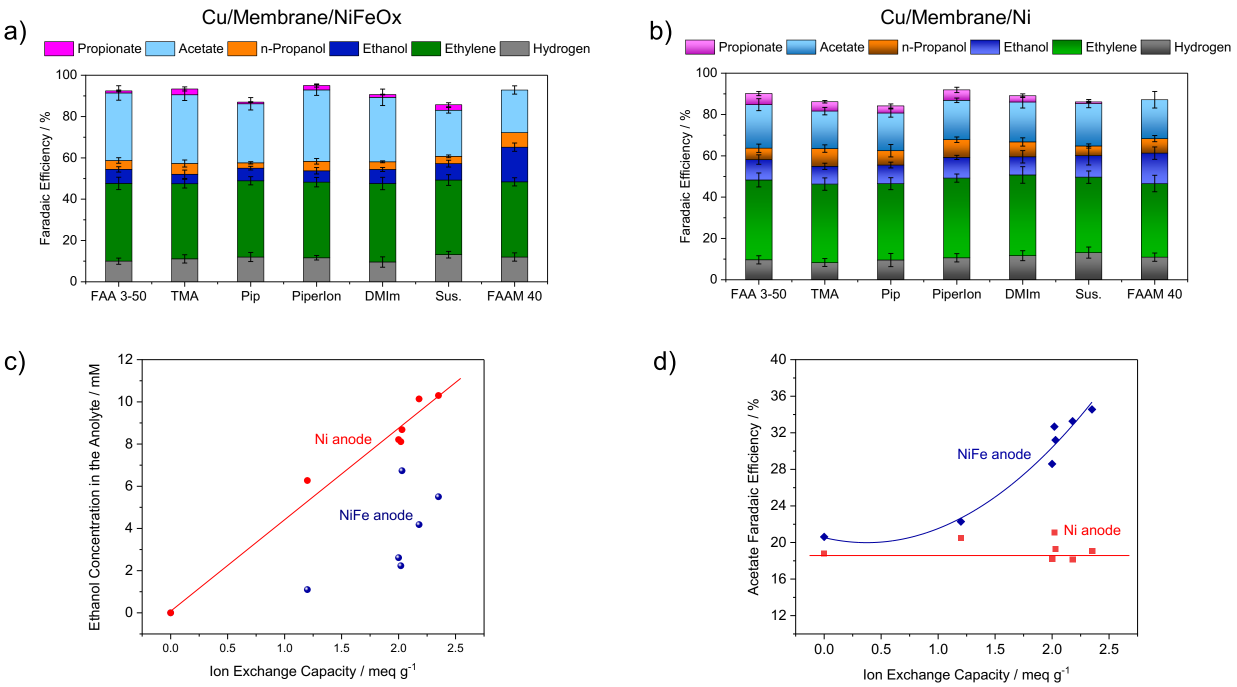

Figure 5. Faradaic efficiencies of various membrane electrode assemblies (MEA's) [6]. A constant current density of 300 mA cm^{-2}, cell temperature of 30^{o}C, CO flow rate 50 mL min^{-1}, and KOH concentration 2 M for (a) Cu/Memb./NiFeOx and (b) Cu/Memb./Ni foam. (c) Ethanol crossover as a function of ion exchange capacity of each membrane. (d) Acetate faradaic efficiency as a function of ion exchange capacity.

We examined the MEA stability using Cu as cathode, various anion exchange membranes, NiFeOx as an anode at 500 mA cm^{-2}, and cell temperature of 30 ^{o}C. The cell stability was evaluated by quantifying product formation every two hours. The total Faradaic efficiencies were higher than 85% over six hours of electrolysis at 500 mA cm^{-2}. In all cases, the hydrogen Faradaic efficiency increased at the expense of ethylene selectivity (Fig. 6a and b). The primary reason for the drop in ethylene production is hydrophobicity loss of the cathode electrode, promoting hydrogen evolution reaction. The MEA with FAA 3-50, Pip, and PiperIon exhibited a slight increase in ethanol Faradaic efficiency of 4% (Fig. 6c). On the other hand, the acetate Faradaic efficiencies dopped by 10, 6, and 8% for FAA 3-50, Pip, and PiperIon, respectively (Fig. 6d). The liquid product selectivity remained constant for all the other MEAs over six hours of electrolysis. The increase in ethanol production can be attributed either to membrane degradation, affecting the alcohol crossover from cathode to anode, or NiFeOx degradation resulting in an inactive catalyst for alcohol oxidation.

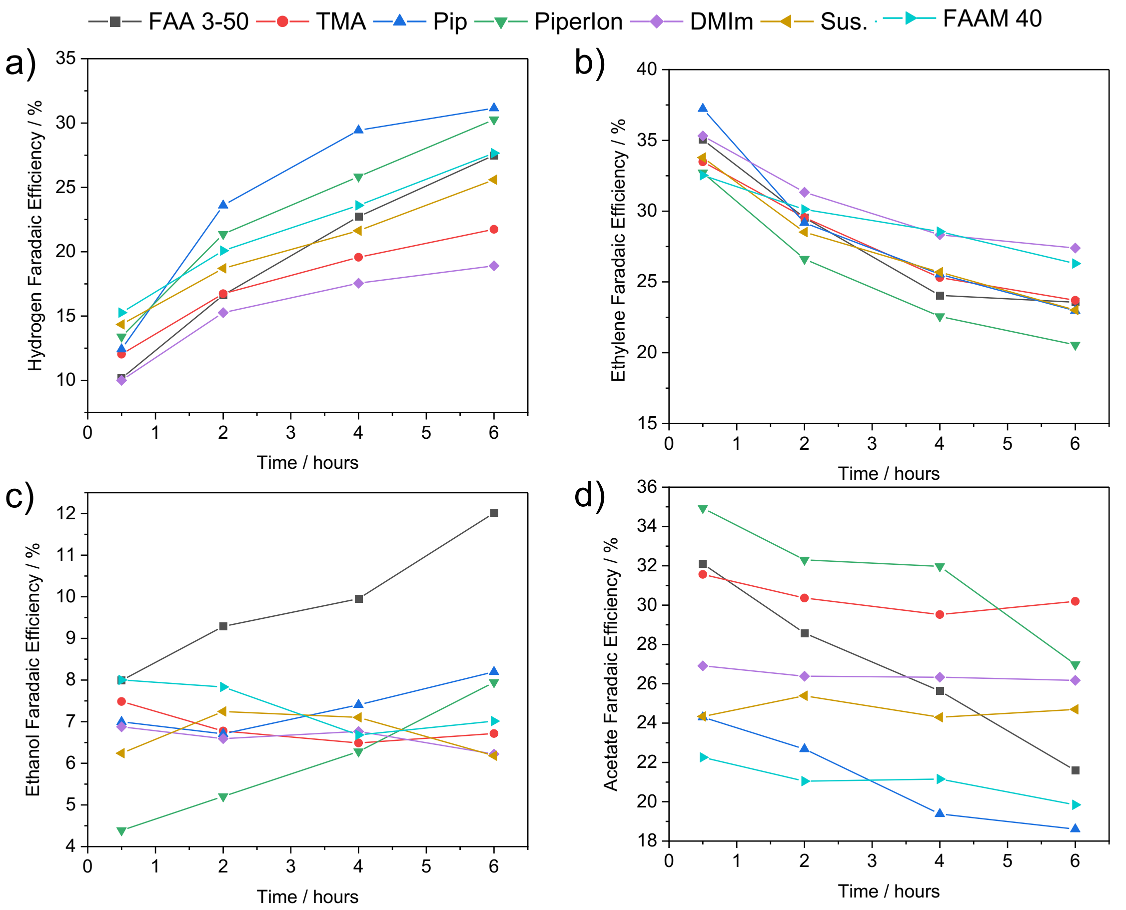

Figure 6. Cell performance over six hours of electrolysis [6]. Experimental conditions: current density of 500 mA cm^{-2}, cell temperature 30 °C, CO flow rate 50 mL min^{-1}, KOH concentration 2 M. Faradaic efficiencies of (a) hydrogen, (b) ethylene, (c) ethanol, and (d) acetate. The different colors correspond to various anion exchange membranes used in an MEA configuration.

The cell potential at a constant current density of 500 mA cm^{-2} degraded from 0.2 to 0.5 mV min^{-1}, dependent on the membrane used in each MEA (Fig. 7a). Both membrane backbone structure and functional group impact the membrane stability. The membrane functional group (quaternary ammonium, imidazolium, piperidine) seems to affect the overall performance. Notably, higher degradation was observed on the membranes with the piperidine functional group such as Pip. and PiperIon. The quaternary ammonium and imidazolium highlighted a lower degradation rate. To deconvolute the contribution of the membrane to the MEA degradation, we conducted a control experiment by changing the cathode and anode after the degradation experiments and having the same membrane (Fig. 7a, top). The cell potential difference (new MEA cell potential from the cell potential at the beginning of the durability experiments) shows that the membrane degradation was less significant to the overall performance. The impact of the cathode and the anode on the cell degradation was most likely more critical in such high applied current density. This control experiment further demonstrated that the piperidine functional group is less stable than imidazolium or quaternary ammonium. Figure 7b shows the images of all the membranes after six hours of electrolysis. The dark area corresponds to the active region where anode and cathode electrodes are placed.

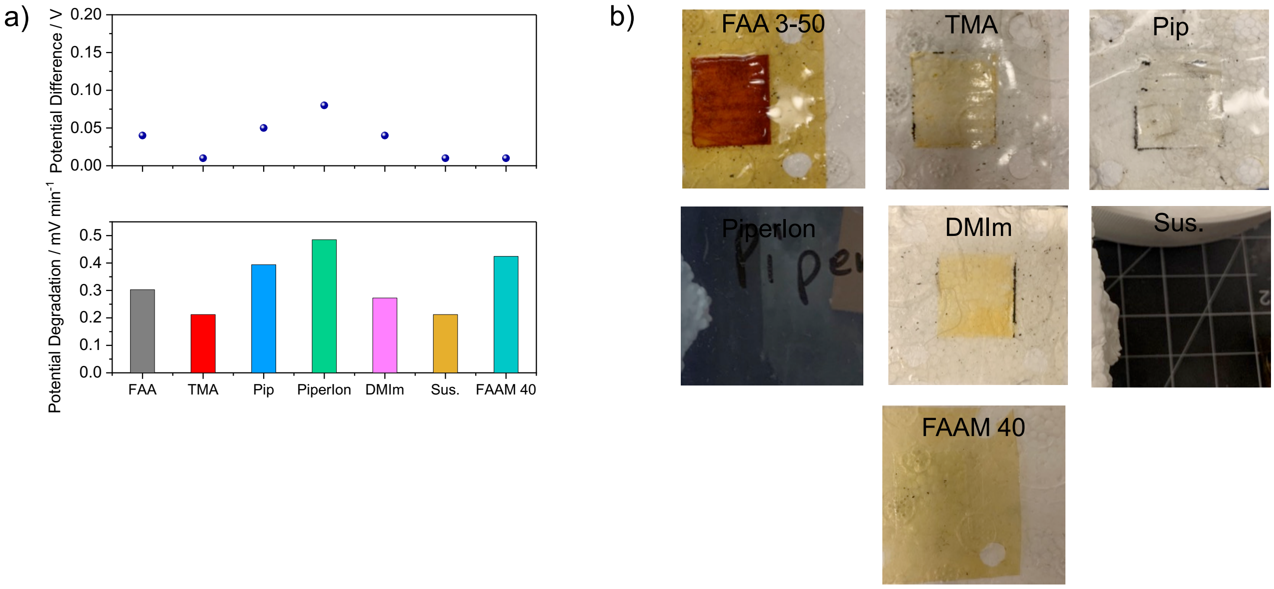

Figure 7. Impact of membranes on electrolyzer degradation [6]. (a) Cell degradation rate (bottom) and the potential difference between the regenerated MEA (new anode and cathode) and the MEA before the six hours of electrolysis. (b) Images of anion exchange membranes after six hours of electrolysis. Experimental conditions: constant current density of 500 mA cm^{-2}, cell temperature 30 °C, CO flow rate 50 mL min^{-1}, KOH concentration 2 M.

At the 5 cm^2 size, interdigited, multi-channel serpentine, and single channel serpentine flow patterns were investigated. All endplates were machined out of 304 Stainless Steel with a flow pattern depth of ~250 microns. For the cathode side, endplates were left as exposed stainless steel due to the reductive conditions inhibiting any formation of iron or nickel oxides. Previous experiments showed no difference between gold coated and non-coated stainless steel cathodes. The prepared endplates are shown in Figure 8 a-c.

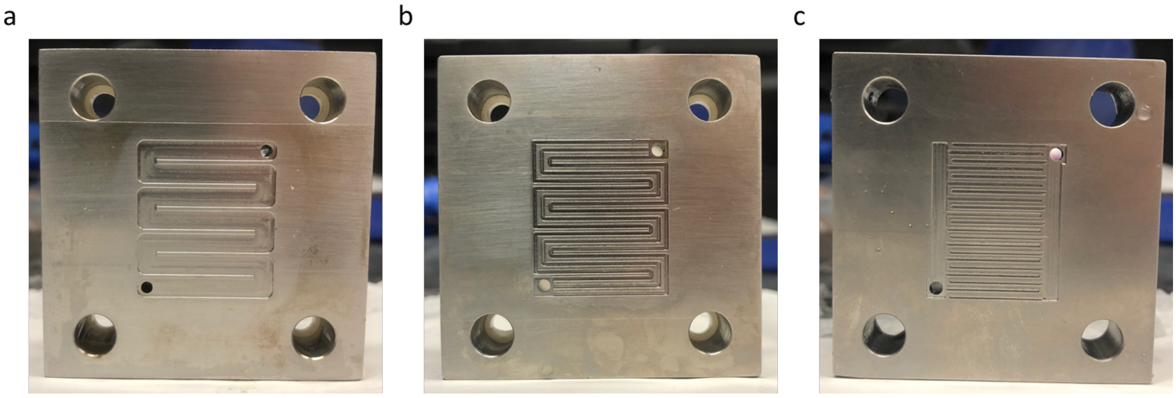

Figure 8. Cathode flow pattern designs. (a) single-channel serpentine, (b) multi-channel serpentine, and (c) interdigited flow patterns.

To investigate the differences between the endplates, the maximum conversion of CO was tested. Operating cell potential, hydrogen Faradaic efficiency, and ethylene Faradaic efficiency were recorded to compare the different flow patterns. It was found that multi-channel serpentine exhibited significantly improved performance over the single-channel and the interdigited designs. A maximum single-pass conversion of CO was achieved at 93% using the multi-channel channel design, whereas the interdigited and single-channel flow fields achieved maximum CO conversions of 84 and 78 % respectively (Fig. 9a). Interdigited and multi-channel serpentine designs had similar cell voltages of 2.34 V and 2.35 V at 84 % conversion, while single-channel serpentine required 2.4 V to achieve 78 % conversion (Fig. 9b). Multi-channel serpentine also maintained the highest production rate of ethylene, which was used as a model product in the experiment, at higher conversions of CO compared to the other two flow patterns (Fig. 9c and d). In conclusion, a multi-channel serpentine flow pattern outperforms other flow patterns and is being manufactured in 25 cm^2 for the durability experiments and for future testing.

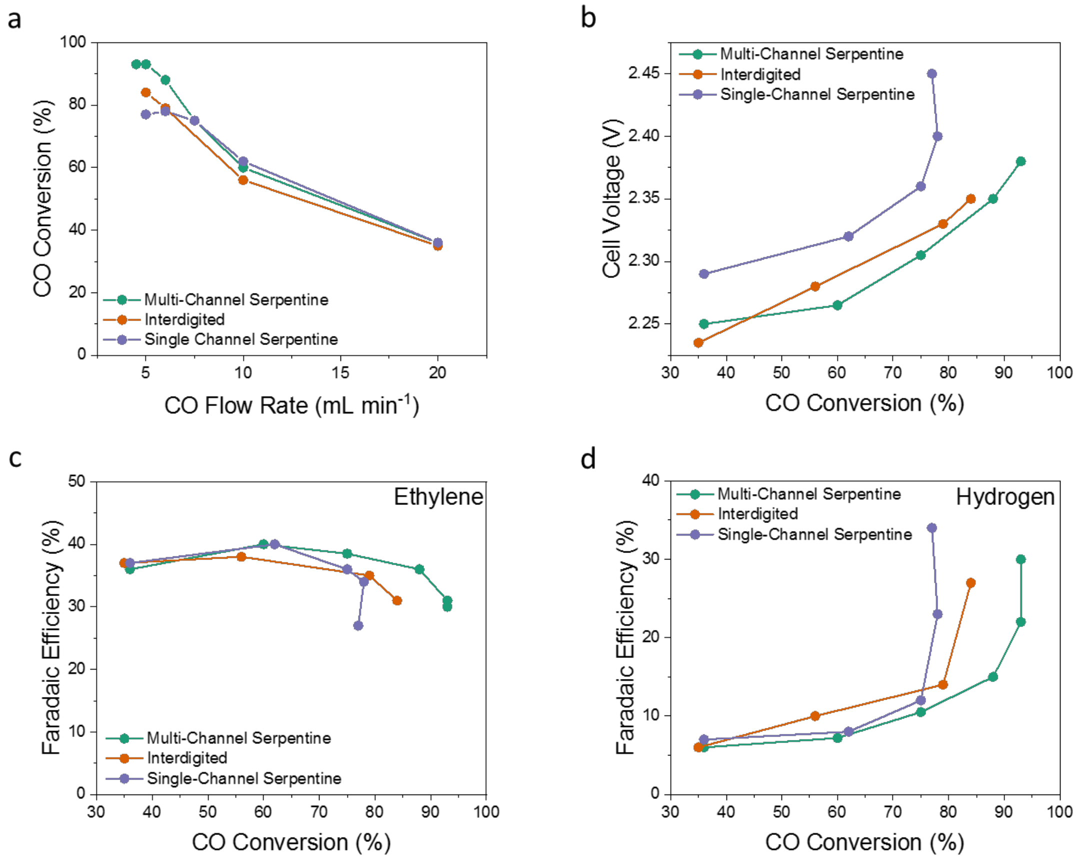

Figure 9. Performance of different flow patterns for the conversion of CO. (a) maximum conversion of CO based on inlet flow rate at 300 mA/cm^2 (total current 1.5 A). (b) operating cell potential at different conversions of CO. (c, d) Faradaic efficiencies of ethylene and hydrogen at increasing CO conversions.

Once the cathode catalyst, membrane design, and flow patterning were investigated, a variety of anodes were studied. One of the key innovations in CO electrolysis reactor design discovered during this study was the ability of the anode to convert undesired alcohols to acetate. To leverage this, a variety of anodes were studied in an H-cell by sweeping from 0.7 to 1.75 V versus reversible hydrogen electrode (RHE) at 25 mV s^{-1}, in 1 M KOH. $NiFeO_x$ anodes were found to be particularly active in the presence of alcohols achieving near 100% selectivity towards carboxylates up to 600 mA cm^{-2} (Fig. 10a). Additional studies were carried out in a flow cell at a partial current density towards C_{2+} products >500 mA cm^{-2} (Fig. 10b). These results also indicated $NiFeO_x$ anodes were the highest performing catalyst of the materials studied.

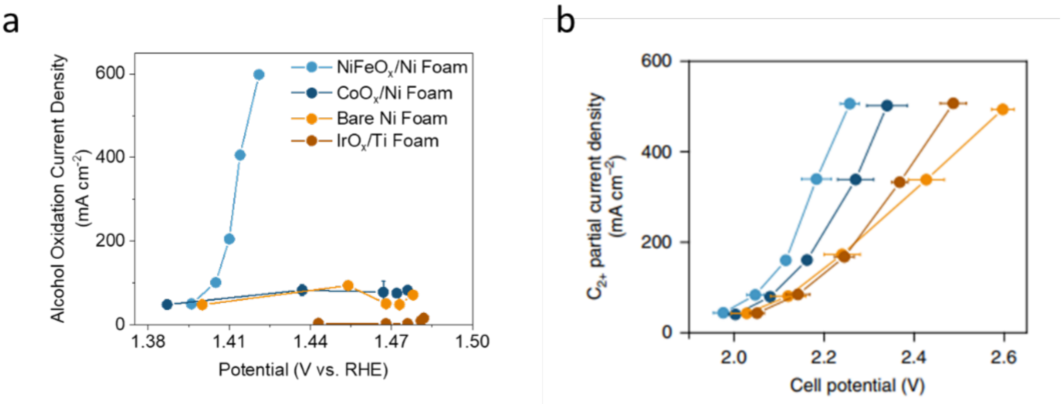

Figure 10. Anodic impact on selectivity via the partial oxidation of alcohols [7]. (a) Partial current density measured for partial oxidation of alcohols to carboxylates. (b) Multicarbon (C_{2+}) partial current density for CO electrolysis performed at 20 sccm CO feed and 2 M KOH using an FAA-3-50 membrane.

With cell hardware and cell components all identified, stability testing was performed in an intermediate-scale 25 cm^2 membrane electrode assembly. Durability of CO electrolyzer was evaluated at an operating condition of 300 mA cm^{-2} in an in-house designed 25 cm^2 electrolyzer. The electrolyzer consisted of a copper nanoparticle cathode (40-60 nm, Sigma Aldrich), an AMX anion exchange membrane (Orion Polymers), and a NiFeO$_x$ anode. AMX was used as the anion exchange membrane, as it is the most recently developed commercial membrane available from Orion Polymers. The cell was operated at ambient conditions and internally self-heated to a temperature of 30°C, due to the internal resistance of the cell. CO was fed to the cathode at a rate of 100 sccm and 2 M KOH was recirculated through the anolyte, replaced every 24 hours. The electrolyzer was operated continuosouly for 100 hours, with gas products analyzed every 4 hours and anolytes analyzed post-recirculation. Initial testing was conducted using a commercially available gas diffusion electrode (Sigracet 39BB) (Fig 11a). However, after about 25 h of operation, hydrogen Faradaic efficiency exceeded 40%.

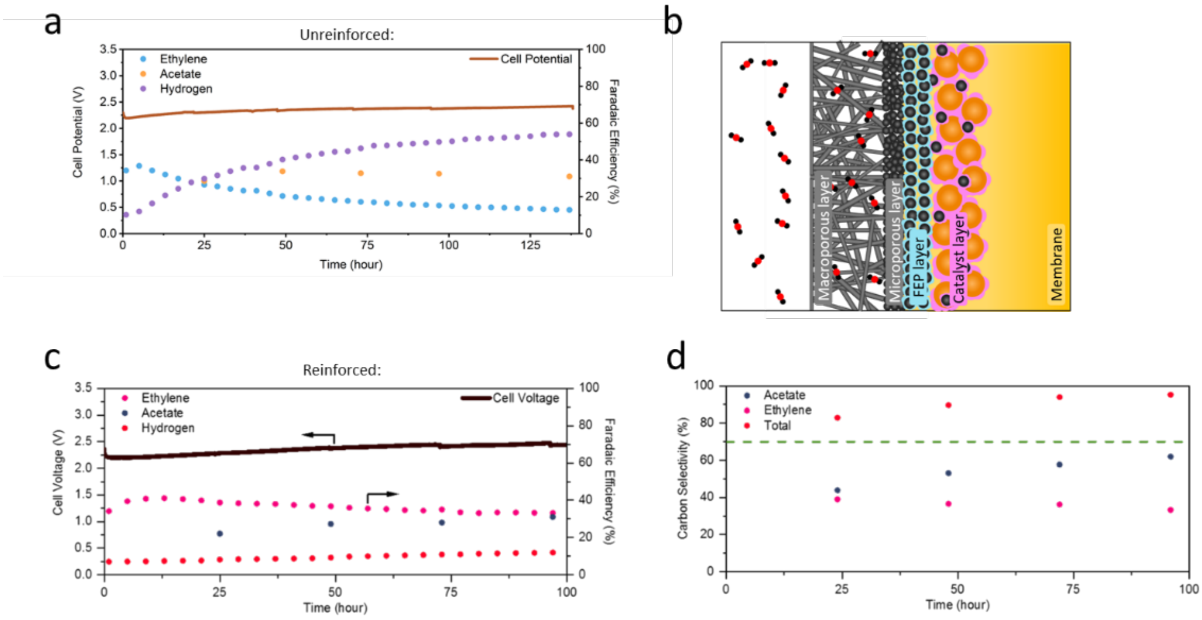

Figure 11. CO electrolysis stability testing. (a) unreinforced gas diffusion electrode stability testing. (b) Schematic of a reinforced gas diffusion electrode. (c) Reinforced gas diffusion electrode stability testing. (d) Reinforced gas diffusion electrode carbon selectivity over time.

To improve stability, the commercial gas diffusion layer was further supported with an improved microporous layer, containing 20% FEPD (Teflon, Fuel Cell Store), to maintain effective CO delivery to the cathode surface (Fig. 11b). The reinforced gas diffusion layer allowed the hydrogen Faradaic efficiency to remain <20% during the course of the 100 h stability test (Fig. 11c). Over the course of the durability experiment, cell voltage maintained a degradation of 2.8 mV/hr, with a minimum voltage of 2.2 V and a maximum voltage of 2.48 V, well below the target cell voltage of 3 V. The cell exhibited an intial rapid degradation, followed by a leveling off. Ethylene Faradaic efficiency was maintained between 33 and 40%. Acetate Faradaic efficiency improved to >30% after the first 48 hours. These efficiencies correspond to a combined carbon selectivity of 83 to 95% over the 100 hours, well in excess of the initial target of 70% (Fig. 11d). Importantly, hydrogen Faradaic efficiency was maintained below 12% over the entire 100 hours, indicating improved durability of the cathode layer and that a majority of the input energy is being directed towards CO reduction instead of water splitting. As a result of this low rate of water splitting, CO conversion was maintained at >40% during the entire experiment.

Development of CO Electrolysis Multi-Cell Stack Reactor

For the entire 10-cell (1,000 cm^2) electrolyzer operation, the system was assembled as two modular 5-cell units (Fig 12a). This setup allowed for improved setup speed and two different catalyst configurations, as will be the case for tandem CO_2-to-CO-to-products system. The entire system includes 2 sets of endplates as well as 10 cathode current collectors made out of 303 stainless steel and 10 anode end plates made from 303 stainless steel (alkaline conditions) or Ti-6Al-4V (neutral/acidic conditions) (Fig. 12b). Cathode endplates utilize a 4 channel serpentine pattern to optimize the gas distribution along the catalyst surface. Anode end plates utilize a parallel flow pattern to optimize O_2 removal from the system. All machined pieces were smoothed to ensure good electrolyzer contact. Cooling channels were integrated throughout the 10cell stack between each cell to allow for heat management which is critical to avoid thermal degradation of the membranes.

Once the stack design was completed, a 500 cm^2 stack was operated as a CO_2 electrolyzer up to a total current of 100 A to supply carbon monoxide downstream to a 1,000 cm^2 CO electrolyzer. The CO_2 electrolyzer demonstrated a relatively high selectivity at scale towards carbon monoxide with <20% Faradaic efficiency lost to hydrogen at each current density studied (Fig. 12c). The 10 cell (1,000 cm^2) CO electrolyzer was successfully operated up to 300 A of total current. At 300 mA cm^{-2}, the CO electrolyzer stack demonstrated relatively low cell voltage of 2.26 V and a relatively high selectivity towards multi-carbons which were primarily acetate and ethylene (Fig. 12d). Small amounts of ethanol, propanol, and propionate were also detected. Similar to smaller-scale tests, the electrolyzer stack was designed so that ethanol and propanol can crossover the membrane from the cathode to the $NiFeO_x$ anode were they are converted to acetate and propionate, respectively. Stability testing on the 1,000 cm^2 CO electrolyzer stack was performed at 300 mA cm^{-2} (Fig. 12e). Good stability was demonstrated up to 125 h and a carbon selectivity >96% has been maintained throughout the experiment, well above the 80% threshold. Cell voltage is also relatively stable at ~2.35 volts (below the 3 V target) and is degrading at a rate of 0.45 mV/h (below the 300 mV/h target). Although ethylene Faradaic efficiency rapidly dropped to ~2% within the first 10 h of the experiment, acetate Faradaic efficiency appears to be stable at ~30%. We attempted to extended the stability test beyond 125 hours (up to ~210 h). However, after 125 h, hydrogen Faradaic efficiency rapidly increased and acetate Faradaic efficiency fell to ~15%. We have completely redesigned the electroylzer hardware to address key issues with the 1st gen stack (compression, flow plate corrosion, flow channel patterning, etc.); however, due to the time and budget constraints, we were not able to test the new generation stack.

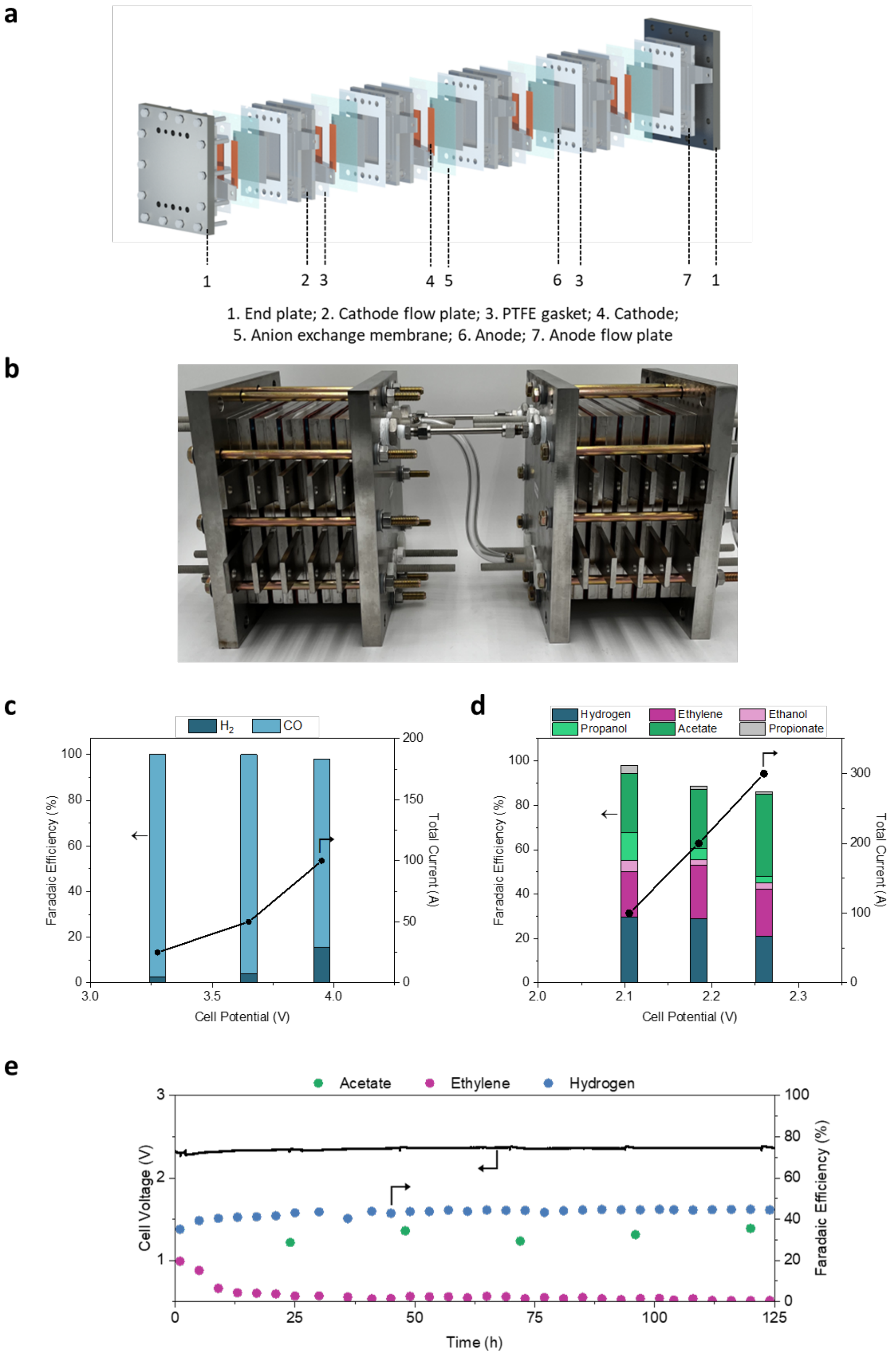

Figure 12. kW-scale CO_2/CO electrolyzer stack. (a) Schematic of one 5-cell stack. (b) Photo of 1,000 cm^2 system composed of two 5-cell stacks. (c) Performance of 500 cm^2 CO_2 electrolyzer stack. (d) Performance of 1,000 cm^2 CO electrolyzer stack. (e) Stability testing of 1,000 cm^2 CO electroylzer stack at 300 mA cm^{-2}.

Once the stack was verified, it was important to consider more realistic conditions prior to further scaling. There are a variety of point sources of CO_2 that can supply a feed gas to a tandem CO_2 electroreduction process. However, the most abundant point source of CO_2 is found in flue gas from natural gas power plants. This CO_2 flue gas stream contains a variety of contaminants such as SO_x, NO_x, O_2, and N_2 that may impact tandem CO_2 electroreduction. Additionally, unreacted CO_2 from the outlet of the CO_2 electrolyzer may be fed downstream to the CO electrolyzer in a tandem system. Even systems that rely on CO_2 sourced from steel production, cement production, or bioprocesses are likely to encounter some of these contaminants. The impact of each impurity needs to be more deeply understood prior to the commercialization of tandem CO_2 electrolysis. To better understand the impact of these anticipated impurities in a large-scale system, SO_2, NO, air, and CO_2 were fed at various concentrations to a CO electrolyzer stack.

Given that some unreacted CO_2 is likely to exit the cathode with CO in a CO_2 electrolyzer, the presence of CO_2 in a CO electrolyzer feed stream must be studied. To better understand how a CO electrolyzer performs in a mixed CO/CO_2 stream, 0-75 vol% CO_2 was introduced to a CO electrolyzer for 30 minutes each (Fig. 13a). Since it is difficult to determine which products came from CO_2 and which came from CO, the number of electron transfers is unknown. Thus, production rate (g h^{-1}) is reported rather than Faradaic efficiency to describe the product distribution. It was demonstrated that as the volume fraction of CO_2 increases in the CO/CO_2 inlet, the product distribution shifts away from acetate and towards hydrogen. When the original pure CO stream is restored following exposure to CO_2, both the acetate production rate declines below its initial performance under pure CO. This is likely due to the formation of (bi)carbonate salt in the electrolyzer which is known to limit performance towards multi-carbons in CO_2 electrolysis. This can also help explain the additional hydrogen formation that is observed in pure CO following CO_2 exposure.

In addition to CO_2, the impact of air on a CO electrolyzer stack was also studied by introducing 0-10 vol% house air the inlet CO stream (Fig. 13b). Relatively little impact was observed on both product distribution and cell voltage when the CO electrolyzer was exposed to up to 10 vol% air. The dominant products throughout the air exposure experiment were acetate and ethylene and hydrogen Faradaic efficiency remained below 15%. There may be some lost Faradaic efficiency due to the oxygen reduction reaction, but these losses appeared to be small (<5%). This indicates that the CO electrolyzer stack has a relatively high resistance to air impurities and that good performance can still be achieved in the presence of air.

The concentration of SO_2 in flue gas can be as high as ~10,000 ppm (~1 vol%), but desulfurized flue gas can reduce this concentration to ~1,000 ppm (~0.1 vol%). To better understand the impact of SO_2 impurities on CO electrolysis, the presence of SO_2 in the CO feed gas was studied across the 0.1-1 vol% concentration range (Fig. 13c). Since Nafion ionomer contains S, FAA ionomer was used so that the SO_2 exposure would be solely responsible for any S detected on the surface of the Cu catalyst. However, FAA ionomer is less hydrophobic than Nafion which led to additional hydrogen formation (30% Faradaic efficiency) prior to SO_2 exposure. Once SO_2 was introduced, hydrogen Faradaic efficiency increased to ~45% and continued to climb to ~55% even once pure CO was reintroduced. XPS analysis revealed that Cu_2S had been formed on the Cu surface which explains the selectivity shift towards hydrogen even once the pure CO has been reintroduced (Fig. 13d).

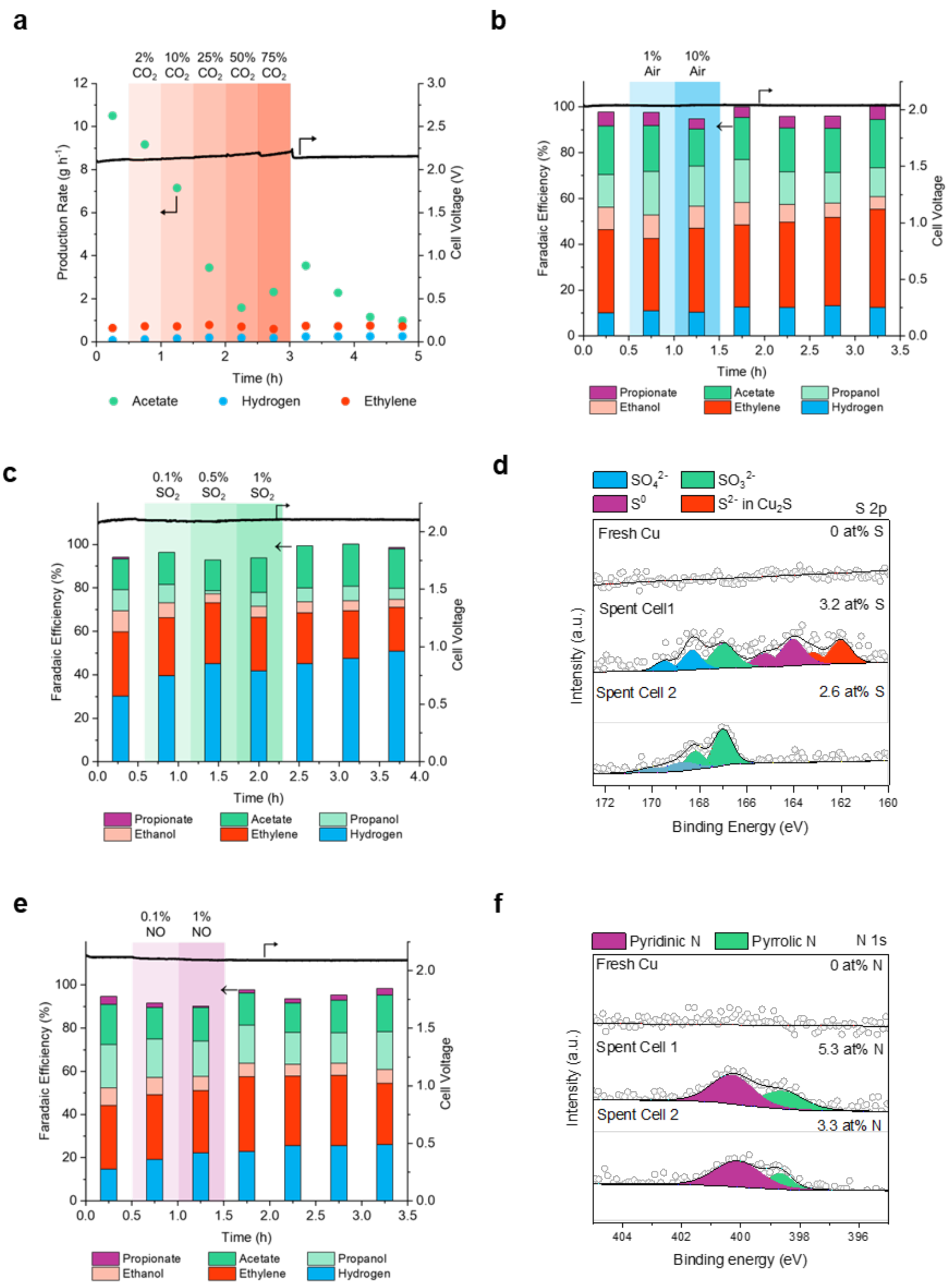

Figure 13. Effect of impurity content in CO electrolysis feed gas. (a) Impact of unreacted CO$_2$ on 2 cell (200 cm^{-2}) CO electrolyzer stack at 100 mA cm^{-2}. (b) Impact of air on 2 cell (200 cm^{-2}) CO electrolyzer stack at 100 mA cm^{-2}. (c) Impact of SO$_2$ on 2 cell (200 cm^{-2}) CO electrolyzer stack at 100 mA cm^{-2}. (d) XPS spectrum of S 2p region on fresh Cu catalysts and on spent Cu catalysts in cell 1 (upstream) and cell 2 (downstream). (e) Impact of NO on 2 cell (200 cm^{-2}) CO electrolyzer stack at 100 mA cm^{-2}. (f) XPS spectrum of S 2p region on fresh Cu catalysts and on spent Cu catalysts in cell 1 (upstream) and cell 2 (downstream).

Previous work has indicated an SO_2-induced selectivity shift towards single carbon products in CO_2 electrolysis [8]. However, no substantial shift in the selectivity towards individual carbon products was detected in CO electrolysis. Throughout the experiment, acetate and ethylene remained the dominant carbon products and cell voltage remained relatively stable. Additionally, previous CO_2 electrolysis work demonstrated a substantial loss in Faradaic efficiency (~20%) under 1% SO_2 exposure [8]. This is expected since SO_2 reduction is more thermodynamically favorable than CO_2/CO reduction (eq 3-7), but the CO electrolyzer stack only lost ~5% Faradaic efficiency. This indicates that the CO electrolyzer stack is relatively resistant to SO_2 contaminants. XPS analysis demonstrated that a greater concentration of S was detected on the surface of Cu in the upstream cell 1 (3.2 at% S) compared to the downstream cell 2 (2.6 at%). Additionally, no S^{2-} in the form of copper (I) sulfide (Cu_2S) or atomic sulfur (S^0) was detected in the downstream cell 2. The only types of S observed in the XPS spectrum for cell 2 was sulfite (SO_3^{2-}) and sulfate (SO_4^{2-}) which were both also observed in cell 1 along with Cu_2S (S^{2-}) and S^0. The sulfites likely formed ex situ as a result of the Cu oxides reacting with SO_2 in the presence of water while the sulfates likely emerged from metal sulfide oxidation. Given that Cu_2S is thermodynamically unstable during electrolysis [8] and cell 2 encountered less SO_2 than the upstream cell 1, it is likely that nearly all of the S^{2-} in the form of Cu_2S was converted to sulfates and sulfites. This indicates that in a large CO electrolyzer stack, the upstream cells will take on the bulk of the sulfur, protecting the downstream cells. These upstream cells could then be continually replaced to enable stable operation.

Besides SO_x, another contaminant typically found in flue gas in NO_x which is most abundant as NO (90-95%) [9]. The content of NO in flue gas typically ranges from 1,000-10,000 ppm (0.1-1 vol%) so this was chosen as the target impurity range in the feed gas to the CO electrolyzer stack. Prior to and during the NO exposure, acetate and ethylene remained the dominant products and cell voltage remained relatively stable (Fig. 13e). A loss in Faradaic efficiency of ~5% under 0.1 vol% NO and ~10% under 1 vol% NO was observed but was fully restored once the pure CO was reintroduced. Previous work has demonstrated that with a Cu catalyst, that these losses are due primarily to the formation of NH_3 and some N_2 [10]. However, the ~5-10% loss in Faradaic efficiency is substantially less than was previously observed (~35%) on Cu in CO_2 electrolysis under similar levels of NO exposure. Like SO_2, some losses in CO_2/CO reduction Faradaic efficiency are expected since NO reduction is more thermodynamically favorable. However, multiple cells in series with large surface areas of Cu helped to mitigate these Faradaic efficiency losses. XPS analysis revealed that the N was bound to the carbon in the GDL in the form of pyrrolic N and Pyridinic N rather than on the Cu catalyst. Additionally, a greater concentration of N appeared on the GDL surface in the upstream cell 1 (5.3 at%) than in the downstream cell 2 (3.3 at%). This indicates that, like in the case of the SO_2 impurities, the upstream cells in an electrolyzer stack will take on the bulk of the contaminants providing protection to the downstream cells (Fig. 13f). Given this and the large catalyst surface area, the CO electrolyzer stack offers relatively good performance in the presence of common flue gas contaminants compared to smaller CO_2 electrolyzers.

Techno-Economic Analysis and Life-Cycle Assessment

This section is intended to build models that bridge the gap between the experimental results and the technology deployed at industrial scale (100 tons/day of acetic acid). The information from tasks 1-4 used in this task is represented in Figure 14.

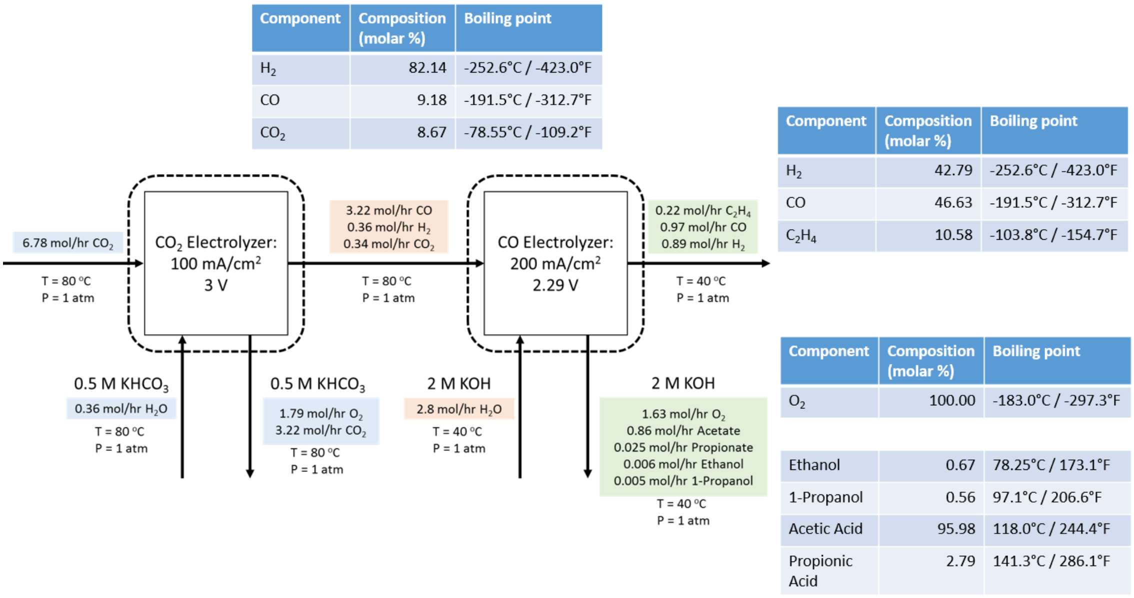

Component	Composition (molar %)	Boiling point
H_2	82.14	-252.6°C / -423.0°F
CO	9.18	-191.5°C / -312.7°F
CO_2	8.67	-78.55°C / -109.2°F

Component	Composition (molar %)	Boiling point
H_2	42.79	-252.6°C / -423.0°F
CO	46.63	-191.5°C / -312.7°F
C_2H_4	10.58	-103.8°C / -154.7°F

Component	Composition (molar %)	Boiling point
O_2	100.00	-183.0°C / -297.3°F
Ethanol	0.67	78.25°C / 173.1°F
1-Propanol	0.56	97.1°C / 206.6°F
Acetic Acid	95.98	118.0°C / 244.4°F
Propionic Acid	2.79	141.3°C / 286.1°F

Figure 14. Data input to the modeling stage.

Previous works on the techno-economic evaluation of CO_2 electroreduction (ECO2R) have focused on single products [11]–[14]. Although experimental research on catalyst design for ECO2R towards C_{2+} products has found wide-ranging distributions of C_1-C_3 products, a systematic understanding of how different product compositions affect the breakeven costs of the technology is still lacking.

Here, we extend the electrolyzer economic models found in the literature [11]–[14] by performing a rigorous mass balance of the systems under study, which will lead to better separation cost estimations in the following section. For each one of the electrolyzer cells (CO_2 reduction into CO, and CO reduction into multi-carbon products), the boundaries of the system are defined and the global mass balance is calculated as in Eq. (1). Eqs. (3(2-(3) correspond to the partial mass balances for each one of the reactions happening in the system, which are used to calculate the outlets of the system.

$$m_{cathode}^{in\ (gas)} + m_{electrolyte}^{in\ (aq)} = m_{cathode}^{out\ (gas)} + m_{electrolyte}^{out\ (aq)} + m_{anode}^{out\ (gas)} \tag{1}$$

$$m_i^j = n_i^j MW_i \tag{2}$$

$$n_i^{out} = n_i^{in} + \Delta n_i \tag{3}$$

$$\Delta n_i = -X_B n_B^0 \left(\frac{\upsilon_i}{\upsilon_B}\right) \tag{4}$$

Thus, the reactions for the two electrolysis stages are defined. Eqs. (5-(10) denote the reactions in alkaline medium at the first cell, including the CO_2 reduction into CO and the formation of hydrogen at the cathode; the carbonate formation and CO_2 recovery in the electrolyte; and the hydroxide oxidation to form water and oxygen.

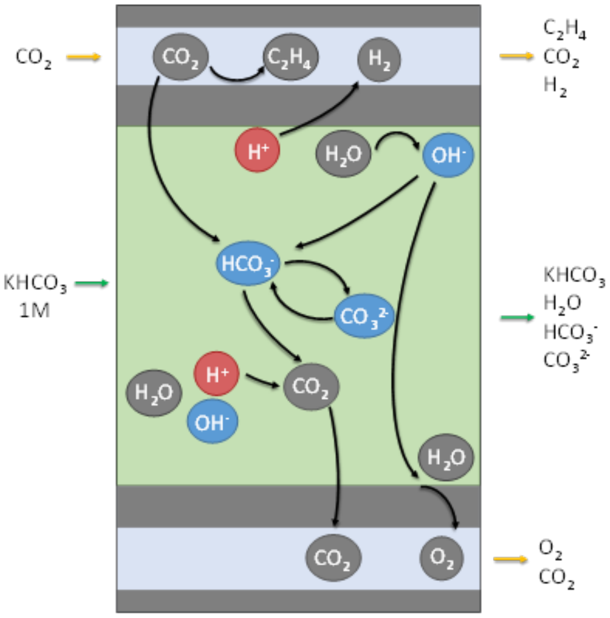

Figure 15. CO$_2$ reduction reactions in the electrolyzer cell.

Cathode:

$CO_2 + H_2O + 2\,e^- \rightarrow CO + 2\,OH^-$ (5)

$2\,H^+ + 2\,e^- \rightarrow H_2$ (6)

Electrolyte:

$CO_2 + OH^- \rightarrow HCO_3^-$ (7)

$HCO_3^- + OH^- \rightarrow CO_3^{2-} + H_2O$ (8)

$H^+ + HCO_3^- \rightarrow CO_2 + H_2O$ (9)

Anode:

$2\,OH^- \rightarrow H_2O + \frac{1}{2}\,O_2 + 2\,e^-$ (10)

Similarly, Eqs. (11-(17) are the reactions for the CO reduction, that yields two gaseous products (ethylene and hydrogen) and four liquid products (ethanol, 1-propanol, acetic acid and propionic acid). Note that, since CO_2 from the first stage is assumed to be removed from the CO stream in a pressure swing adsorber, carbonate formation is not considered.

Cathode:

$$2\,CO + 6\,H_2O + 8\,e^- \rightarrow C_2H_4 + 8\,OH^- \tag{11}$$

$$2\,H^+ + 2\,e^- \rightarrow H_2 \tag{12}$$

$$2\,CO + 7\,H_2O + 8\,e^- \rightarrow C_2H_5OH + 8\,OH^- \tag{13}$$

$$3\,CO + 10\,H_2O + 12\,e^- \rightarrow C_3H_7OH + 12\,OH^- \tag{14}$$

$$2\,CO + 4\,H_2O + 4\,e^- \rightarrow CH_3COOH + 4\,OH^- \tag{15}$$

$$3\,CO + 7\,H_2O + 8\,e^- \rightarrow C_2H_5COOH + 8\,OH^- \tag{16}$$

Anode:

$$2\,OH^- \rightarrow H_2O + \frac{1}{2}\,O_2 + 2\,e^- \tag{17}$$

Table 1. shows the resulting partial mass flows at each one of the inlet and outlet streams to process 10 tonnes per hour of CO_2. The variables from the experimental results at the previous tasks used to characterize the conversion of the reactants into the products are: the single-pass conversion, the faradaic efficiencies (product selectivities), the water excess, and the carbonate formation and recovery ratios (

Table **2**).

Table 1. Partial mass flows at the inlets and outlets to process 10 tonnes/h of CO_2.

Mass flows [tonne/h]	CO_2 Reduction		CO Reduction	
Cathode inlet	CO_2	10.00	CO	3.02
Electrolyte inlet	H_2O	6.14	H_2O	6.14
	$KHCO_3$	1M	KOH	2M
Cathode outlet	CO_2	0.50	CO	0.91
	CO	3.02	H_2	0.04
	H_2	0.02	C_2H_4	0.20
Electrolyte outlet	H_2O	5.92	H_2O	5.92
	$KHCO_3$		KOH	
			C_2H_5OH	0.01
			C_3H_7OH	0.01
			CH_3COOH	1.70
			C_2H_5COOH	0.09
Anode outlet	CO_2	4.75	O_2	0.74
	O_2	1.92		

Table 2. Operational variables from the experimental results used in this assessment.

Variable	CO_2 Reduction	CO Reduction
Cell voltage [V]	3.00	2.29
Current density [mA/cm^2]	100	200

Single-pass conversion [%]	47.5		70.0	
Faradaic efficiencies [%]			H_2	15.5
			C_2H_4	25.1
	CO	90.0	C_2H_5OH	0.7
	H_2	10.0	$C_3H_7O\ H$	0.8
			CH_3COOH	49.8
			C_2H_5COOH	4.4
Water excess ratio	1.5		1.5	
Carbonate formation [%]	47.5%		-	
Carbonate recovery [%]	100%		-	

As observed in Table 1, the main product of the two-step reduction is 22wt% acetic acid that needs to be purified from the water and traces of other products present in the electrolyte outlet. Purifying acetic acid from a mix with water to market quality (99% purity for glacial acetic acid) by conventional distillation is an energy intensive process, and avoided due to the small separating factor of the mixture. For dilute solutions of acetic acid in water (i.e., at or below 30 wt % = 11.5 mol % acetic acid), hybrid separation using liquid−liquid extraction followed by distillation is often used [15]. Ethyl acetate is used as the extraction agent. The process is modeled the process in Aspen Plus (Fig. 16) and consists of an extraction tower, a rectification tower for the recovery of the extraction agent, and the water-stripping tower.

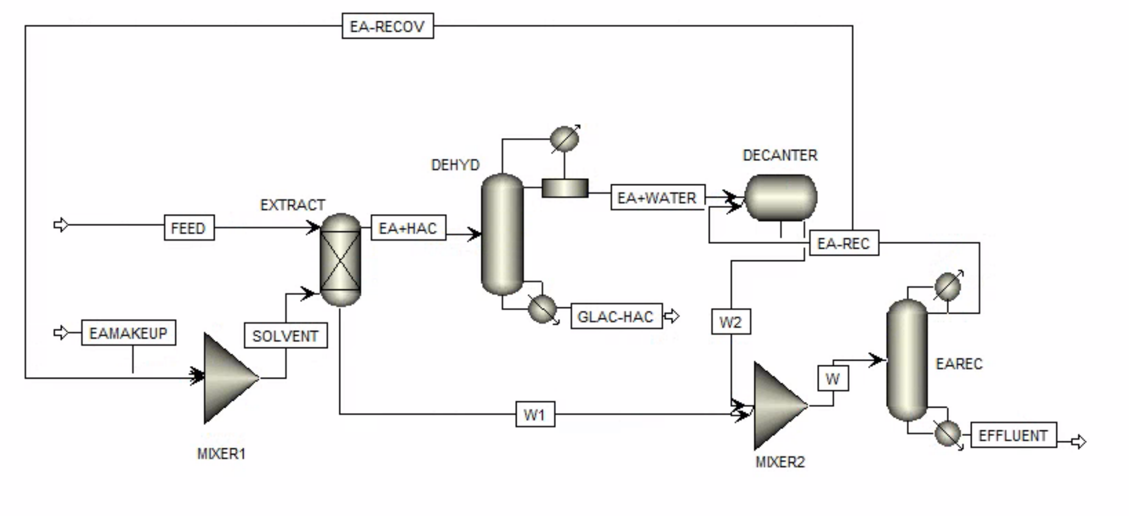

Figure 16. Flowsheet of the process to purify acetic acid.

The techno-economic assessment of the two-stage process includes the price of the inlet CO_2 and other utilities, and the capital and operational costs of the electrolysis and gas and liquid separations as represented in Figure 16. The separation of the gas products from CO_2 and CO are done in pressure swing adsorbers. Since the main components of the liquid outlet are water and acetic acid, the liquid separation costs are gathered from a contribution on the extractive distillation of a stream with similar composition (70% water and 30% acetic acid) [16]. The cost parameters of the electrolyzer and the pressure swing adsorber are retrieved from former techno-economic assessments of ECO2R. All the cost parameters and assumptions used in this assessment are summarized in Table 3.

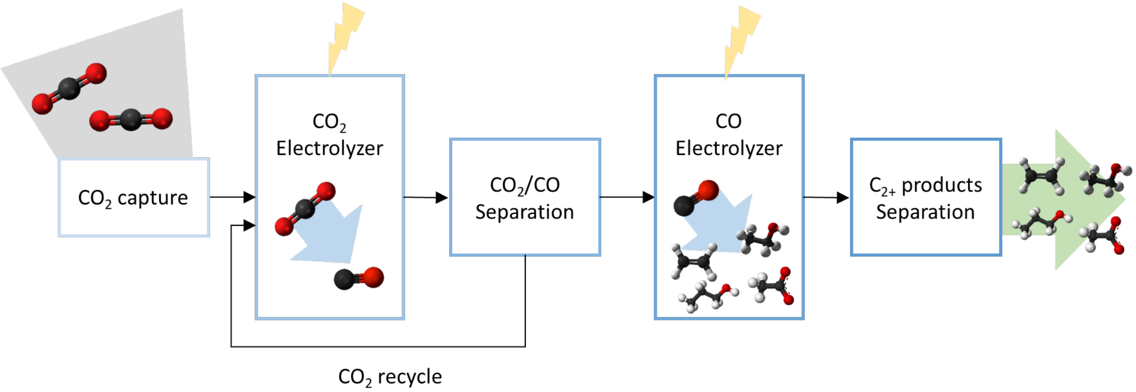

Figure 17. Diagram of the two-stage CO_2 reduction into C_{2+} products.

Table 3. Economic parameters and assumptions.

Cost	Value	Reference
CO_2 Cost	40 USD/tonne	[12]
Electricity Cost	30 USD/MWh	[12]
Electrolyzer Reference Cost	450 USD/kW	[17]
Electrolyzer Lifetime	20 years	[12]
Electrolyzer Maintenance Cost	2.5% of the electrolyzer annual capex	[17]
Electrolyzer Replacement Cost	15% of the electrolyzer annual capex	[17]
Catalyst and Membrane Cost	5% of the electrolyzer capex	[13]
Catalyst and Membrane Lifetime	5 years	[13]
Membrane Replacement Cost	25% of the electrolyzer annual capex	[17]
PSA Reference Cost	1.99 M USD	[18]
PSA Reference Flowrate	1000 m^3/h	[18]
PSA Scaling Factor	0.70	[12]
PSA Electric Consumption	0.25 kWh/m^3	[18]
PSA Lifetime	20 years	[18]
Distillation Reference Cost	1.20 M$	[16]
Distillation Reference Flowrate	75 l/min	[16]
Distillation Scaling Factor	0.70	[12]
Distillation Opex	4658 $/day	[16]
Distillation Lifetime	20 years	[12]
Discount Rate	7 %	[13]

The annual and unitary costs resulting from the TEA are shown in
Table **4**

Table **5**.

Table 4. Annual and unitary cost breakdowns for the electroreduction of CO_2 into CO.

Cost breakdown	Annual cost [$/year]	Unitary cost [$/tonne acetic acid]	Cost contribution [%]
CO_2 Input Cost	4,077,780.00	111.59	20.15
Water Input	23,169.20	0.63	0.11
Electricity Cost	12,419,337.23	339.85	61.38
Electrolyzer Capex	501,839.72	13.73	2.48
Catalyst/Membrane Capex	64,832.21	1.77	0.32
Electrolyzer Maintenance Cost	229,489.93	6.28	1.13
PSA Cathode Opex	517,025.58	14.15	2.56
PSA Cathode Capex	795,694.36	21.77	3.93
PSA Anode Opex	660,948.44	18.09	3.27
PSA Anode Capex	944,942.04	25.86	4.67
TOTAL	20235058.71	553.72	100.00

Table 5. Annual and unitary cost breakdowns for the electroreduction of CO into acetic acid.

Cost breakdown	Annual cost [$/year]	Unitary cost [$/tonne acetic acid]	Cost contribution [%]
Water Input	303,140.39	8.30	1.64
Electricity Cost	8,662,259.65	237.04	46.79
Electrolyzer Capex	700,047.97	19.16	3.78
Catalyst/Membrane Capex	90,438.55	2.47	0.49
Electrolyzer Maintenance Cost	320,130.03	8.76	1.73
PSA Cathode Opex	224,278.18	6.14	1.21
PSA Cathode Capex	443,443.99	12.13	2.40
PSA Anode Opex	90,981.56	2.49	0.49
PSA Anode Capex	235,806.21	6.45	1.27
Distillation Cathode Opex	7,133,272.35	195.20	38.53
Distillation Cathode Capex	309,106.84	8.46	1.67
TOTAL	18,512,905.72	506.60	100.00

Figure 18 shows the cost breakdown in USD per tonne of acetic acid. The price range of CO and acetic acid in the U.S. between 2016 and 2020 was also included to assess how far the breakeven costs of both technologies are from the market price. While the reduction of CO_2 into CO would be cost competitive showing modest to inexistent profits depending on the market price, the production of acetic acid would be far from viable implementation with a total cost of $1205 (note that the CO_2 reduction costs have to be added to the CO reduction to consider the total cost of the two-stage process). The main driver of both processes is the cost of the electricity to power the electrolyzer (a 60% of the total cost for the CO_2 reduction and a 46% at the CO reduction). The next higher contributions are from the CO_2 capture and electrolyzer maintenance costs for the CO_2 reduction and the extractive distillation opex and electrolyzer maintenance costs for the CO reduction.

In Figure 19, we perform a sensitivity analysis of these cost drivers on the total cost of the two-stage process. Even in the most optimistic case that the four cost drivers could be reduced a 25%, the total cost to produce acetic acid would be higher than the market price.

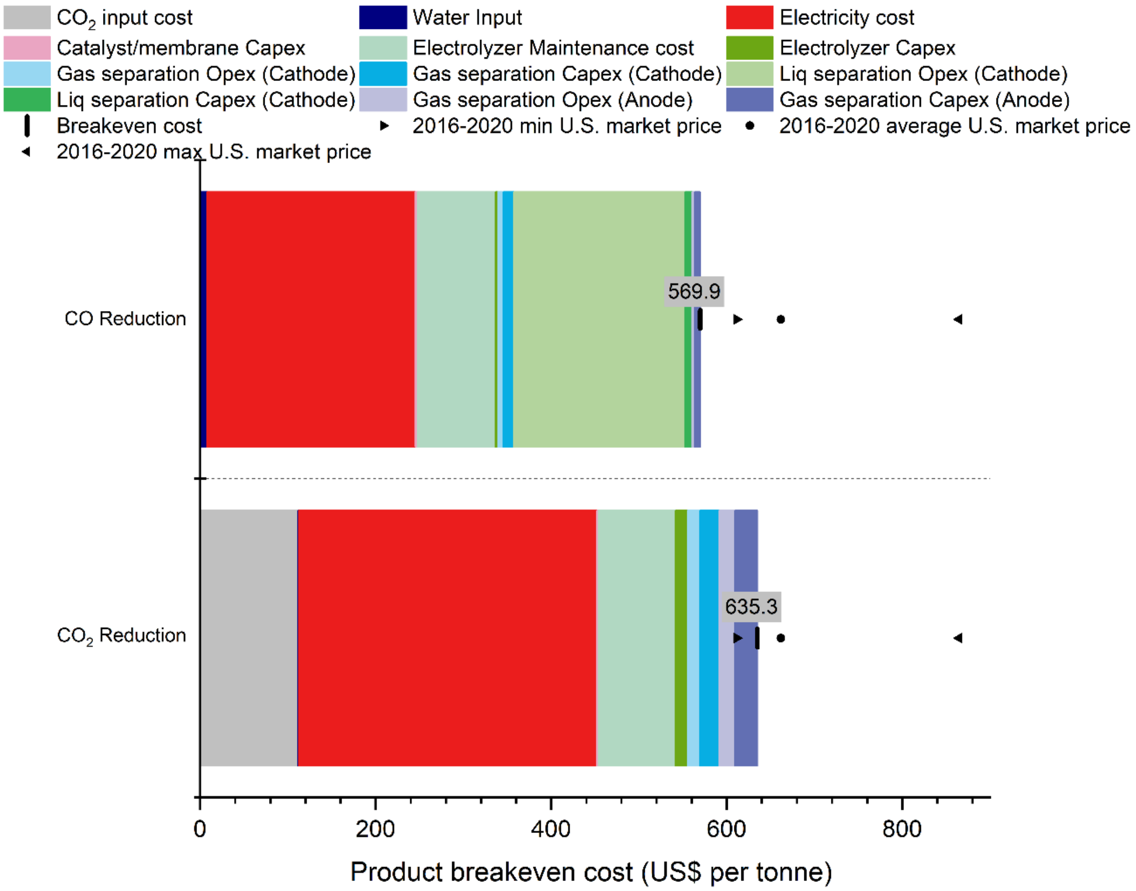

Figure 18. Cost breakdown for the two stages of the electroreduction of CO_2 into acetic acid.

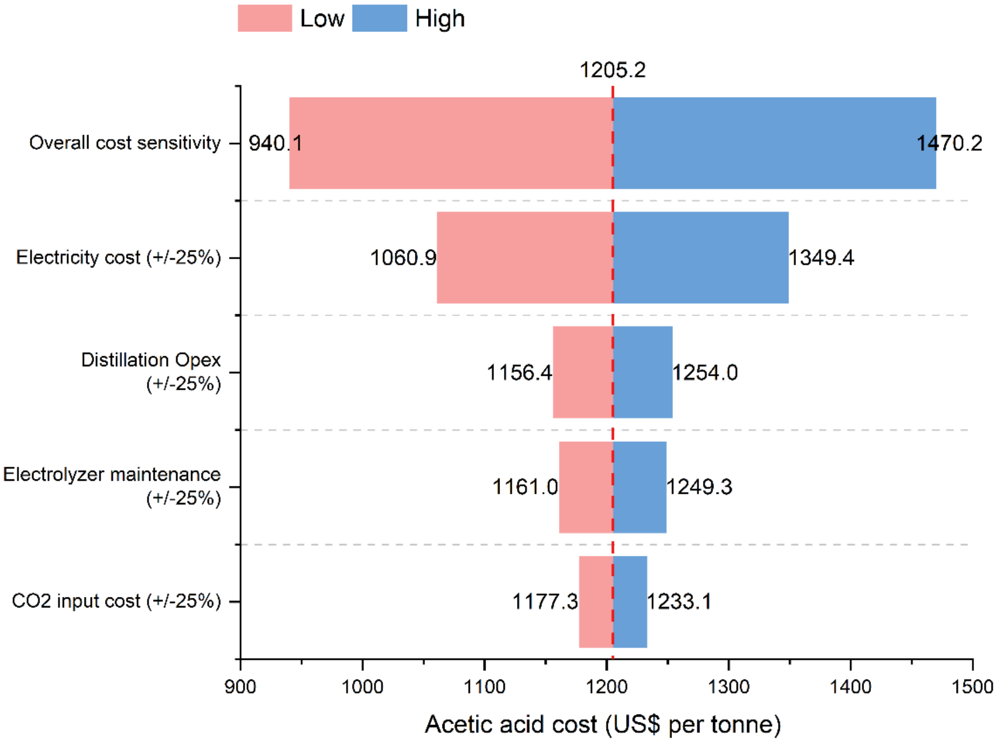

Figure 19. Sensitivity analysis on the total cost of producing acetic acid through the two-step electroreduction route over the electricity cost, the CO_2 cost, the electrolyzer maintenance and the distillation opex.

The goal of this LCA is defined in the following terms:

- Intended application: To assess the environmental impacts of the main product (acetic acid) of the electroreduction of CO_2, and compare it against the business as usual (BAU) process for its chemical manufacturing.
- Reasons for conducting the study: To evaluate the environmental performance of the emerging technology of the electroreduction of CO_2 as an alternative to manufacture chemicals.
- Intended audience of the study: The scientific community working on the electroreduction of CO_2.
- Public disclosure:
- Potential limitations: This study is limited to the assumptions used when modeling the technology (see section 5.0).
- Study commissioner:

The scope:

- Functional unit: The functional unit used is 1 kg of acetic acid, to which all the calculations are referred.
- System boundaries: A cradle-to-gate study is performed, from the capture of CO_2 to the outlet of the electroreduction and purification. Since the final product has the same structure than its conventional counterpart, their downstream phases (transport, use and end of life) will be identical and thus do not have to be included in the study.

- Management of co-products: A system expansion is applied and, due to the low concentration of the by-products of the process (mainly carbon monoxide and ethylene), they will be included as credits for their avoided production through a conventional route.
- Geographical and time representation: When available, the most recent data for the U.S. mix will be considered.

The system boundaries are represented in Figure 20. The mass balances are adjusted to the production of 1kg of acetic acid in Table 6. The net flows of the process for the functional unit and the entries used to model them are shown in
Table 7.

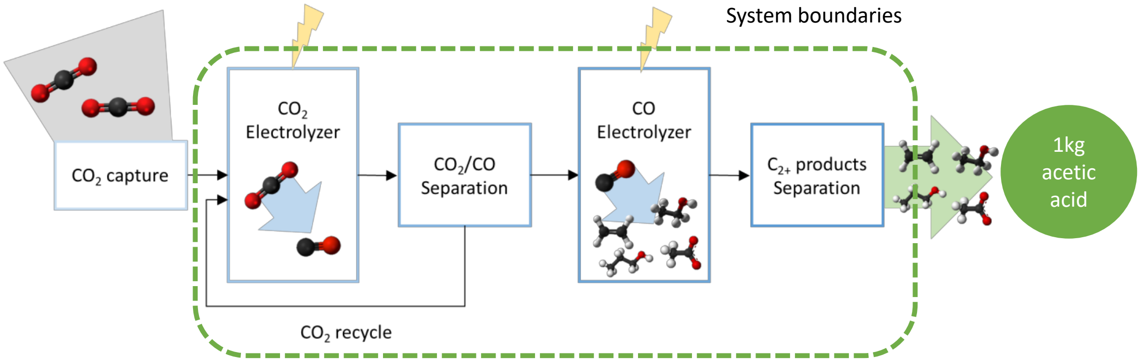

Figure 20. System boundaries.

Table 6. Mass balances adjusted to the functional unit.

Mass flows [tonne/h]	CO_2 Reduction		CO Reduction	
Cathode inlet	CO_2	5.88	CO	1.78
Electrolyte inlet	H_2O	3.61	H_2O	3.61
	$KHCO_3$	-	KOH	-
Cathode outlet	CO_2	0.29	CO	0.54
	CO	1.78	H_2	0.02
	H_2	0.01	C_2H_4	0.12
Electrolyte outlet	H_2O	3.48	H_2O	3.48
	$KHCO_3$		KOH	
			C_2H_5OH	0.01
			C_3H_7OH	0.01
			CH_3COOH	1.00
			C_2H_5COOH	0.05
Anode outlet	CO_2	2.79	O_2	0.44
	O_2	1.13		

Table 7. Net flows of the process per kg of acetic acid and associated USLCI entries.

	Amount	Unit	USLCI entry
Products			

Acetic acid	1.0000	kg	“Acetic acid, at plant”
Carbon monoxide	0.5328	kg	“Carbon monoxide, at plant”
Ethanol	0.0054	kg	“Ethanol, denatured, corn stover, biochemical”
Ethylene	0.1177	kg	“Ethylene, at plant”
1-propanol	0.0054	kg	-
Propionic acid	0.0539	kg	-
Raw materials			
Ethyl acetate	0.0120	kg	*“Ethyl acetate {GLO}| maket for | APOS, S”
Water	8.7390	kg	“Water, fresh”
Utilities			
Electricity – CO2R	11.3283	kWh	“Electricity; at user; consumption mix - US - US” *“Electricity, medium voltage, renewable energy products {CH}| market for electricity, medium voltage, renewable energy products | APOS, S”
Electricity – PSA Anode CO2R	0.4716	kWh	
Electricity – PSA Cathode CO2R	0.6029	kWh	
Electricity – COR	7.9013	kWh	
Electricity – PSA Anode COR	0.2046	kWh	
Electricity – PSA Cathode COR	0.0830	kWh	
Electricity – AAD_EA	0.0300	kWh	
Heat – AAD_EA	1.2010	kWh	*”Heat, district or industrial, natural gas {GLO}| market group for | APOS, S”
Emissions			
O_2 Emissions	1.5616	kg	“Oxygen”
Water Outlet	6.9535	kg	“Water”

*Entries from EcoInvent v3.8.

The results of the two-step electrosynthesis of acetic acid are compared to the traditional (BAU business as usual) route to produce acetic acid and both cases are evaluated using the current electricity mix and 100% renewable. Thus, the four scenarios evaluated are:

- BAU + GRID: Business as usual production of acetic acid with the current electricity mix.
- BAU + REN: Business as usual production of acetic acid powered by renewable energy.
- ECO2R + GRID: Electrocatalytic production of acetic acid with the current electricity mix.
- ECO2R + REN: Electrocatalytic production of acetic acid powered by renewable energy.

The results for these scenarios are shown in Table 8 and Figure 21.

Table 8. Global warming impact [kg CO2 eq/kg acetic acid] per scenario.

Scenario	Process emissions	Raw materials	Electricity	Natural gas	Other	Avoided emissions
BAU + GRID	0.0018	0.6744	0.0179	0.7245	0.0020	0.0000
BAU + REN	0.0018	0.6744	0.0003	0.7245	0.0020	0.0000

ECO2R + GRID	0.0000	0.0333	16.0589	0.2740	0.0000	-2.7897
ECO2R + REN	0.0000	0.0329	0.2220	0.2740	0.0000	-2.7897

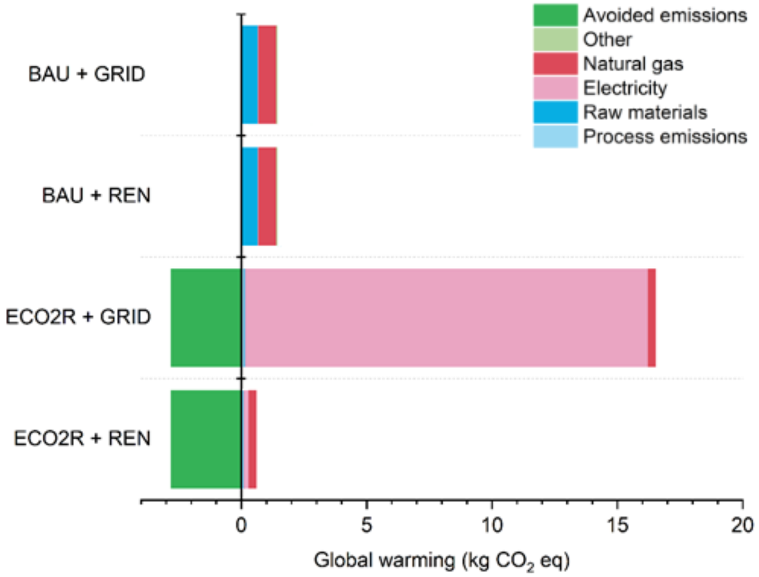

Figure 21. Global warming impact in kg CO_2 eq per kg of acetic acid for the four different scenarios.

4. CONCLUSION

In conclusion, a two-step CO_2 electroreduction process for selective production of acetate and ethylene was successfully developed at the kW-scale. The CO_2 and CO electrolyzers were first investigated individually on the Watt-scale to achieve high current densities and more durable operation by using a reinforced GDL. High CO_2 conversion was obtained in the first CO_2 electrolyzer to produce a CO-dominant gas stream with minimal CO_2, and highly pure acetate stream was produced in the second CO electrolyzer by using NiFe anode, which promoted alcohol oxidation to carboxylates. The two-step process operated stably for 200 h with acetate and ethylene as the major C_{2+} products. Degradation mechanism study revealed that the flooding and the salt formation in the GDL is likely the biggest contributor to the performance degradation for both CO_2 and CO electrolyzers.

A 1,000 cm^2 CO electrolyzer stack was then designed, fabricated, and operated up to a total current of 300 A along with a 500 cm^2 CO_2 electrolyzer stack which was operated up to a total current of 100 A. The CO electrolyzer stack demonstrated good stability at 300 A for at least 125 h at a carbon selectivity >96%. The impact of CO_2, O_2, N_2, SO_x, and NO_x gas impurities on the CO electrolyzer stack was studied and a relatively high resistance to these contaminants was demonstrated. Electroreduction of CO_2 into acetic acid was also demonstrated to be environmentally favorable when compared to the traditional production of acetic acid when powered by renewable electricity. Additionally, electricity cost was identified as the primary source of cost sensitivity indicating substantial economic improvements could be achieved by continuing to drive down the cost of renewable electricity. Overall, the presented approach demonstrates the feasibility of the two-step electrochemical CO_2 reduction process for the effective production of C_{2+} products at the kW-scale which should inspire future scaling efforts accelerating commercialization.

5. MILESTONES

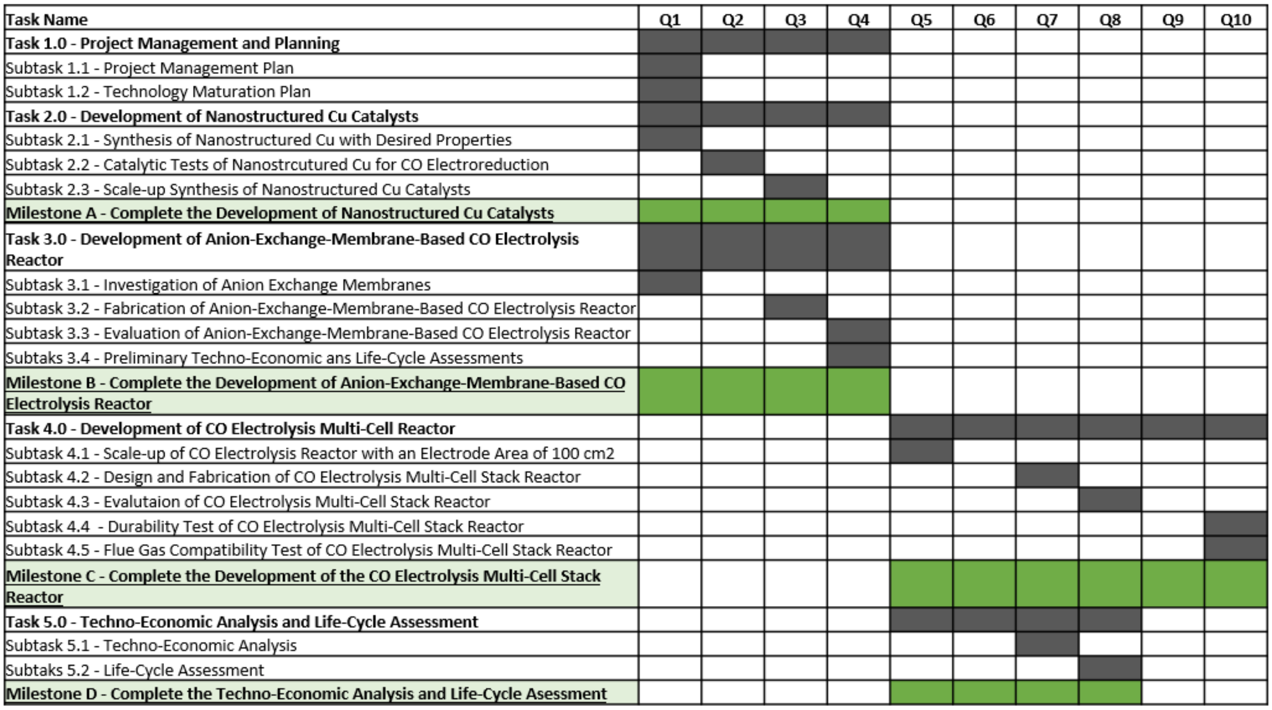

Task Name	Q1	Q2	Q3	Q4	Q5	Q6	Q7	Q8	Q9	Q10
Task 1.0 - Project Management and Planning	■	■	■	■						
Subtask 1.1 - Project Management Plan	■									
Subtask 1.2 - Technology Maturation Plan	■									
Task 2.0 - Development of Nanostructured Cu Catalysts	■	■	■	■						
Subtask 2.1 - Synthesis of Nanostructured Cu with Desired Properties	■									
Subtask 2.2 - Catalytic Tests of Nanostrcutured Cu for CO Electroreduction		■								
Subtask 2.3 - Scale-up Synthesis of Nanostructured Cu Catalysts			■							
Milestone A - Complete the Development of Nanostructured Cu Catalysts	🟩	🟩	🟩	🟩						
Task 3.0 - Development of Anion-Exchange-Membrane-Based CO Electrolysis Reactor	■	■	■	■						
Subtask 3.1 - Investigation of Anion Exchange Membranes	■									
Subtask 3.2 - Fabrication of Anion-Exchange-Membrane-Based CO Electrolysis Reactor			■							
Subtask 3.3 - Evaluation of Anion-Exchange-Membrane-Based CO Electrolysis Reactor				■						
Subtaks 3.4 - Preliminary Techno-Economic ans Life-Cycle Assessments				■						
Milestone B - Complete the Development of Anion-Exchange-Membrane-Based CO Electrolysis Reactor	🟩	🟩	🟩	🟩						
Task 4.0 - Development of CO Electrolysis Multi-Cell Reactor					■	■	■	■	■	■
Subtask 4.1 - Scale-up of CO Electrolysis Reactor with an Electrode Area of 100 cm2					■					
Subtask 4.2 - Design and Fabrication of CO Electrolysis Multi-Cell Stack Reactor							■			
Subtask 4.3 - Evalutaion of CO Electrolysis Multi-Cell Stack Reactor								■		
Subtask 4.4 - Durability Test of CO Electrolysis Multi-Cell Stack Reactor										■
Subtask 4.5 - Flue Gas Compatibility Test of CO Electrolysis Multi-Cell Stack Reactor										■
Milestone C - Complete the Development of the CO Electrolysis Multi-Cell Stack Reactor					🟩	🟩	🟩	🟩	🟩	🟩
Task 5.0 - Techno-Economic Analysis and Life-Cycle Assessment					■	■	■	■		
Subtask 5.1 - Techno-Economic Analysis							■			
Subtaks 5.2 - Life-Cycle Assessment								■		
Milestone D - Complete the Techno-Economic Analysis and Life-Cycle Asessment					🟩	🟩	🟩	🟩		

6. REFERENCES

1. ISO 14044: Life Cycle Assessment — Requirements and Guidelines, 2006.
2. A. Zimmermann *et al.*, Techno-Economic Assessment & Life Cycle Assessment Guidelines for CO_2 Utilization (Version 1.1). 2020.
3. L. J. Müller, A. Kätelhön, M. Bachmann, A. Zimmermann, A. Sternberg, and A. Bardow. A Guideline for Life Cycle Assessment of Carbon Capture and Utilization. *Front. Energy Res.*, 2020, **8**.
4. Luc, W. *et al.* Two-dimensional copper nanosheets for electrochemical reduction of carbon monoxide to acetate. *Nat. Catal.* 2019, **2**: p. 423-430.
5. Ha, T. H., Koo, H. J. & Chung, B. H. Shape-controlled syntheses of gold nanoprisms and nanorods influenced by specific adsorption of halide ions. *J. Phys. Chem. C* 2007, **111**: p. 1123–1130.
6. Hasa, B., Cherniack, L., Xia, R., Tian, D., Ko, B.H., Overa, S., Dimitrakellis, P., Bae, C., Jiao, F. Benchmarking anion-exchange membranes for electrocatalytic carbon monoxide reduction. *Chem Catalysis*, 2023, **3**: 100450.

7. Overa, S., Crandall, B. S., Shrimant, B., Tian, D., Ko, B. H., Shin, H., Bae, C., Jiao, F. Enhancing acetate selectivity by coupling anodic oxidation in carbon monoxide electroreduction. *Nature Catalysis*, 2022, **5**: p. 738–745.
8. Luc., W., Ko, B. H., Kattel, S., Li, S., Su, D., Chen, J. G., Jiao, F. SO_2-Induced Selectivity Change in CO_2 Electroreduction. *J. Am. Chem. Soc.* 2019, **25**: p. 9902-9909.
9. Gholami, F., Tomas, M., Gholami, Z. & Vakili, M. Technologies for the nitrogen oxides reduction from flue gas: a review. *Sci. Total Environ.* 2020, **714**: 136712.
10. Ko, B. H., Hasa, B., Shin, H., Jeng, E., Overa, S., Chen, W., Jiao, F. The impact of nitrogen oxides on electrochemical carbon dioxide reduction. *Nat. Comm*. 2020, **11**: 5856.
11. M. Rumayor, A. Dominguez-Ramos, P. Perez, and A. Irabien, “A techno-economic evaluation approach to the electrochemical reduction of CO2 for formic acid manufacture,” *J. CO2 Util.*, 2019, **34**: p. 490–499.
12. H. Shin, K. U. Hansen, and F. Jiao, “Techno-economic assessment of low-temperature carbon dioxide electrolysis,” *Nat. Sustain.*, 2021, **4**: p. 911-918.
13. J. Sisler *et al.*, “Ethylene Electrosynthesis: A Comparative Techno-economic Analysis of Alkaline vs Membrane Electrode Assembly vs CO 2 –CO–C 2 H 4 Tandems,” *ACS Energy Lett.*, 2021, **6**: p. 997-1002.
14. M. J. Orella, S. M. Brown, M. E. Leonard, Y. Román-Leshkov, and F. R. Brushett, “A General Technoeconomic Model for Evaluating Emerging Electrolytic Processes,” *Energy Technol.*, 2019: 1900994.
15. A. Lucia, A. Amale, and R. Taylor, “Energy Efficient Hybrid Separation Processes,” *Ind. Eng. Chem. Res.*, 2006, **45**: p. 8319–8328.
16. G. R. Harvianto, K. J. Kang, and M. Lee, “Process Design and Optimization of an Acetic Acid Recovery System in Terephthalic Acid Production via Hybrid Extraction–Distillation Using a Novel Mixed Solvent,” *Ind. Eng. Chem. Res.*, 2017, **56**: p. 2168–2176.
17. B. James, W. Colella, J. Moton, G. Saur, and T. Ramsden, “PEM Electrolysis H2A Production Case Study Documentation, NREL/TP-5400-61387,” Golden, Colorado, 2013.
18. M. Jouny, W. Luc, and F. Jiao, “High-rate electroreduction of carbon monoxide to multi-carbon products,” *Nat. Catal.*, 2018, **1**: p. 748–755.

7. PRODUCTS

a. Publications, conference papers, and presentations

i. Journal publications

(1) Crandall, B. S., Overa, S., Shin, H., Jiao, F. Turning carbon dioxide into sustainable food and chemicals: how electrosynthesized acetate is paving the way for fermentation innovation. *Accounts of Chemical Research*, 2023, **56**: p. 1505-1516.

(2) Hasa, B., Cherniack, L., Xia, R., Tian, D., Ko, B.H., Overa, S., Dimitrakellis, P., Bae, C., Jiao, F. Benchmarking anion-exchange membranes for electrocatalytic carbon monoxide reduction. *Chem Catalysis*, 2023, **3**: 100450

(3) Overa, S., Crandall, B. S., Shrimant, B., Tian, D., Ko, B. H., Shin, H., Bae, C., Jiao, F. Enhancing acetate selectivity by coupling anodic oxidation in carbon monoxide electroreduction. *Nature Catalysis*, 2022, **5**: p. 738–745.

(4) Overa, S., Ko, B. H., Zhao, Y., Jiao, F. Electrochemical Approaches for CO_2 Conversion to Chemicals: A Journey toward Practical Applications. *Accounts of Chemical Research*, 2022, **55**: p. 638–648.

(5) Ko, B. H., Hasa, B., Shin, H., Zhao, Y., Jiao, F. Electrochemical Reduction of Gaseous Nitrogen Oxides on Transition Metals at Ambient Conditions. *Journal of the American Chemical Society*, 2022, **144**: p. 1258–1266.
(6) Shin, H., Hansen, K. U., Jiao, F. Techno-economic assessment of low-temperature carbon dioxide electrolysis. *Nature Sustainability*, 2021, **4**: p. 911–919

ii. Presentations

(1) Crandall, B. S., Jiao, F. kW-Scale Tandem CO_2 Electroreduction to Multi-Carbons. North American Catalysis Society 28th Meeting. Providence, RI. June 23, 2023.

iii. Patents

N/A

8. PARTICIPANTS & OTHER COLLABORATING ORGANIZATIONS (optional)

N/A

9. IMPACT (optional)

N/A

10. CHANGES/PROBLEMS

None.

11. SPECIAL REPORTING REQUIREMENTS

None.

12. BUDGETARY INFORMATION

Below is the final budgetary information including the cost share status.

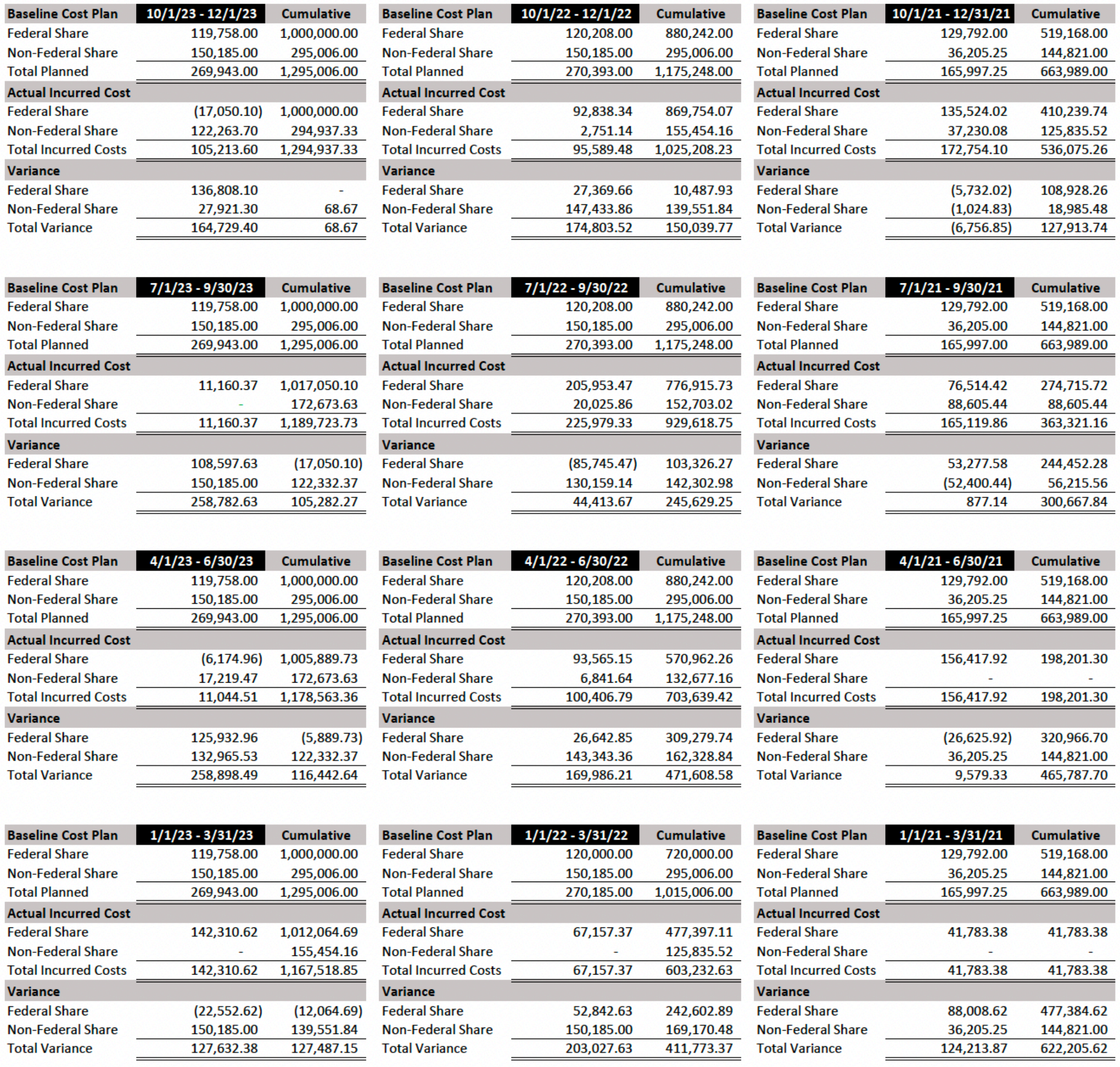

Baseline Cost Plan	10/1/23 - 12/1/23	Cumulative
Federal Share	119,758.00	1,000,000.00
Non-Federal Share	150,185.00	295,006.00
Total Planned	269,943.00	1,295,006.00
Actual Incurred Cost		
Federal Share	(17,050.10)	1,000,000.00
Non-Federal Share	122,263.70	294,937.33
Total Incurred Costs	105,213.60	1,294,937.33
Variance		
Federal Share	136,808.10	-
Non-Federal Share	27,921.30	68.67
Total Variance	164,729.40	68.67

Baseline Cost Plan	10/1/22 - 12/1/22	Cumulative
Federal Share	120,208.00	880,242.00
Non-Federal Share	150,185.00	295,006.00
Total Planned	270,393.00	1,175,248.00
Actual Incurred Cost		
Federal Share	92,838.34	869,754.07
Non-Federal Share	2,751.14	155,454.16
Total Incurred Costs	95,589.48	1,025,208.23
Variance		
Federal Share	27,369.66	10,487.93
Non-Federal Share	147,433.86	139,551.84
Total Variance	174,803.52	150,039.77

Baseline Cost Plan	10/1/21 - 12/31/21	Cumulative
Federal Share	129,792.00	519,168.00
Non-Federal Share	36,205.25	144,821.00
Total Planned	165,997.25	663,989.00
Actual Incurred Cost		
Federal Share	135,524.02	410,239.74
Non-Federal Share	37,230.08	125,835.52
Total Incurred Costs	172,754.10	536,075.26
Variance		
Federal Share	(5,732.02)	108,928.26
Non-Federal Share	(1,024.83)	18,985.48
Total Variance	(6,756.85)	127,913.74

Baseline Cost Plan	7/1/23 - 9/30/23	Cumulative
Federal Share	119,758.00	1,000,000.00
Non-Federal Share	150,185.00	295,006.00
Total Planned	269,943.00	1,295,006.00
Actual Incurred Cost		
Federal Share	11,160.37	1,017,050.10
Non-Federal Share	-	172,673.63
Total Incurred Costs	11,160.37	1,189,723.73
Variance		
Federal Share	108,597.63	(17,050.10)
Non-Federal Share	150,185.00	122,332.37
Total Variance	258,782.63	105,282.27

Baseline Cost Plan	7/1/22 - 9/30/22	Cumulative
Federal Share	120,208.00	880,242.00
Non-Federal Share	150,185.00	295,006.00
Total Planned	270,393.00	1,175,248.00
Actual Incurred Cost		
Federal Share	205,953.47	776,915.73
Non-Federal Share	20,025.86	152,703.02
Total Incurred Costs	225,979.33	929,618.75
Variance		
Federal Share	(85,745.47)	103,326.27
Non-Federal Share	130,159.14	142,302.98
Total Variance	44,413.67	245,629.25

Baseline Cost Plan	7/1/21 - 9/30/21	Cumulative
Federal Share	129,792.00	519,168.00
Non-Federal Share	36,205.00	144,821.00
Total Planned	165,997.00	663,989.00
Actual Incurred Cost		
Federal Share	76,514.42	274,715.72
Non-Federal Share	88,605.44	88,605.44
Total Incurred Costs	165,119.86	363,321.16
Variance		
Federal Share	53,277.58	244,452.28
Non-Federal Share	(52,400.44)	56,215.56
Total Variance	877.14	300,667.84

Baseline Cost Plan	4/1/23 - 6/30/23	Cumulative
Federal Share	119,758.00	1,000,000.00
Non-Federal Share	150,185.00	295,006.00
Total Planned	269,943.00	1,295,006.00
Actual Incurred Cost		
Federal Share	(6,174.96)	1,005,889.73
Non-Federal Share	17,219.47	172,673.63
Total Incurred Costs	11,044.51	1,178,563.36
Variance		
Federal Share	125,932.96	(5,889.73)
Non-Federal Share	132,965.53	122,332.37
Total Variance	258,898.49	116,442.64

Baseline Cost Plan	4/1/22 - 6/30/22	Cumulative
Federal Share	120,208.00	880,242.00
Non-Federal Share	150,185.00	295,006.00
Total Planned	270,393.00	1,175,248.00
Actual Incurred Cost		
Federal Share	93,565.15	570,962.26
Non-Federal Share	6,841.64	132,677.16
Total Incurred Costs	100,406.79	703,639.42
Variance		
Federal Share	26,642.85	309,279.74
Non-Federal Share	143,343.36	162,328.84
Total Variance	169,986.21	471,608.58

Baseline Cost Plan	4/1/21 - 6/30/21	Cumulative
Federal Share	129,792.00	519,168.00
Non-Federal Share	36,205.25	144,821.00
Total Planned	165,997.25	663,989.00
Actual Incurred Cost		
Federal Share	156,417.92	198,201.30
Non-Federal Share	-	-
Total Incurred Costs	156,417.92	198,201.30
Variance		
Federal Share	(26,625.92)	320,966.70
Non-Federal Share	36,205.25	144,821.00
Total Variance	9,579.33	465,787.70

Baseline Cost Plan	1/1/23 - 3/31/23	Cumulative
Federal Share	119,758.00	1,000,000.00
Non-Federal Share	150,185.00	295,006.00
Total Planned	269,943.00	1,295,006.00
Actual Incurred Cost		
Federal Share	142,310.62	1,012,064.69
Non-Federal Share	-	155,454.16
Total Incurred Costs	142,310.62	1,167,518.85
Variance		
Federal Share	(22,552.62)	(12,064.69)
Non-Federal Share	150,185.00	139,551.84
Total Variance	127,632.38	127,487.15

Baseline Cost Plan	1/1/22 - 3/31/22	Cumulative
Federal Share	120,000.00	720,000.00
Non-Federal Share	150,185.00	295,006.00
Total Planned	270,185.00	1,015,006.00
Actual Incurred Cost		
Federal Share	67,157.37	477,397.11
Non-Federal Share	-	125,835.52
Total Incurred Costs	67,157.37	603,232.63
Variance		
Federal Share	52,842.63	242,602.89
Non-Federal Share	150,185.00	169,170.48
Total Variance	203,027.63	411,773.37

Baseline Cost Plan	1/1/21 - 3/31/21	Cumulative
Federal Share	129,792.00	519,168.00
Non-Federal Share	36,205.25	144,821.00
Total Planned	165,997.25	663,989.00
Actual Incurred Cost		
Federal Share	41,783.38	41,783.38
Non-Federal Share	-	-
Total Incurred Costs	41,783.38	41,783.38
Variance		
Federal Share	88,008.62	477,384.62
Non-Federal Share	36,205.25	144,821.00
Total Variance	124,213.87	622,205.62